# Detecting magmatic-derived fluids using pyrite chemistry: example of the Chibougamau area, Abitibi Subprovince, Québec

Lucie Mathieu[a,*]

[a] UQAC institutional Chair on Archean metallogenic processes, Centre d'études sur les Ressources minérales (CERM), Département des Sciences appliquées, Université du Québec à Chicoutimi (UQAC), 555 boul. de l'université, Chicoutimi, G7H 2B1 QC, Canada, lucie1.mathieu@uqac.ca

*Corresponding author: lucie1.mathieu@uqac.ca; Tel: (+001)-418-545-5011 ext. 2538

Submitted as a regular paper to

Ore Geology Reviews

**Abstract**

Magmatic fluids are an important carrier of precious and base metals in many mineralized systems (porphyry deposits, intrusion-related gold systems – IRGS, volcanogenic massive sulfides – VMS). Recognizing magmatic inputs is essential for understanding metallogenic processes and for developing accurate exploration models, and the importance of fluids exsolved from magmas remains a source of much debate for some contexts, such as IRGS and orogenic gold deposits. This study aims to identify magmatic fluids in the Chibougamau area (northeastern corner of the Neoarchean Abitibi Subprovince, Canada), using pyrite chemistry. This is achieved by comparing the chemistry of pyrites recovered from the Cu-Au magmatic-hydrothermal (porphyry) systems of the Chibougamau area to "background" compositions, i.e., the chemistry of pyrites from weakly mineralized rocks from the same area. Analyses of quantitative laser ablation inductively coupled plasma mass spectrometry (LA-ICP-MS) are processed in three distinct manners to better evaluate the trace elements controlled by silicates, oxides, sulfides, and sulfosalt inclusions and the trace elements that are structurally bound to pyrite. Detailed investigation of the trace element content of pyrite indicates that most elements are controlled by silicate inclusions, some reflect the composition of the host rock, others correlate with the mineralizing style, and only Te and Bi are discriminant of the porphyry systems of the Chibougamau area. Tellurium is structurally bound to pyrite or forms telluride nanoparticles in the study area, while the distribution of Bi is controlled by galena and chalcopyrite inclusions, and pyrite chemistry is interpreted using absolute Te values and Bi ratios (Bi/Pb and Bi/Cu). This study provides insight into the Cu-Au magmatic-hydrothermal systems of the Chibougamau area. It also has implications for the way pyrite chemistry can be used to probe for magmatic fluids in other mineralized contexts.

**Keywords:** pyrite chemistry; Te-Bi, porphyry deposit; magmatic-hydrothermal systems; Abitibi Subprovince; fluid signature

## 1. Introduction

Many gold and base metal Archean mineralization are related to hydrothermal systems dominated by heated seawater (VMS, volcanogenic massive sulfides) or metamorphic fluids (orogenic gold deposits) (Galley et al., 2007; Hannington et al., 2005; Phillips and Powell, 2010). The influx of magmatic fluids in most of these systems is progressively being recognized; for example, the input of magmatic fluid may upgrade gold in VMS (Mercier-Langevin et al., 2011) or form early low-grade mineralization that are later remobilized and upgraded by orogenic gold systems (Meffre et al., 2016). Magmatic fluids also dominate the gold-mineralizing processes that occur late in the evolution of a greenstone belt, i.e., intrusion-related gold systems (IRGS), also referred to as syenite-associated types (Robert, 2001). Other Archean magmatic-hydrothermal systems concentrate gold and base metals. They form during the main magmatic phase of greenstone belts and are designated as porphyry deposits. Examples of such systems include the Côté-Gold Au ±Cu deposit in Ontario (Katz et al., 2017), as well as the Lac Bachelor Au and the Central Camp Cu-Au deposits in Québec (Fayol and Jébrak, 2017; Mathieu and Racicot, 2019).

Thus, magmatic fluids are an essential component of Archean gold and base metal deposits. Determining the origin of hydrothermal fluids is useful for classifying deposits, understanding their genesis, and vectorizing in an exploration context (Huston et al., 1995). For example, from an exploration point of view, an intermediate to felsic magma intrusion may host the mineralization, i.e., intrusion with a passive role (Robert and Poulsen, 1999). Intrusions may have a more active role, as metals may be leached from igneous rocks by an hydrothermal system, or molten magmas may exsolve metal-bearing fluids. In the latter cases, intermediate to felsic intrusions are the source of metals and the chemistry of the intrusive rocks may be worth integrating within an exploration model. The lack of recognition of magmatic fluid inputs is thus detrimental to our understanding of metallogenic processes and their application within exploration models.

Magmatic fluids are identified readily when the mineralized system comprises hydrothermal breccia, intermineral dikes (dikes that cut and are cut by the mineralization), and specific alteration (Na- and/or K-metasomatism), as observed in the Central Camp Cu-

Au porphyry system (Cimon, 1973; Guha et al., 1984; Pilote et al., 1996). In other systems, the importance of magmatic fluid influx remains debated, such as in the Malartic gold deposit, which is either an IRGS (Helt et al., 2014) or an orogenic gold system partially hosted by felsic intrusions (De Souza et al., 2016). The IRGS deposits can be recognized from metal assemblages (Cu, Pb, Zn, Mo, W, Te, Bi, As, F, B) (Duuring et al., 2007; Robert, 2001) that are not usually observed in gold-only orogenic deposits (Phillips and Powell, 2010). This implies that the chemistry of magmatic fluids differs from that of heated seawater and from metamorphic fluids that have interacted with magmatic rocks at an elevated fluid/rock ratio.

This study aims to evaluate the usefulness of pyrite chemistry as a probe for assessing magmatic fluid influx into mineralizing systems. Pyrite is abundant in hydrothermal systems; it can incorporate high levels of many trace elements, and its chemistry has been studied intensely (Deditius et al., 2011; Large et al., 2009; Roberts, 1982). Pyrite is useful to metallogenists because of its abundance, its capacity to integrate metals and non-metals and because one of the main factors controlling metal uptake in pyrite is the chemical composition of the hydrothermal fluid (Deditius and Reich, 2016). There is, however, no simple correlation between the source of a fluid, its chemistry, and the chemistry of associated hydrothermal pyrite, and it is essential to take into account the properties of pyrite and study how pyrite incorporates metals before concluding on the chemistry of the hydrothermal fluid with which pyrite may have equilibrated (Chouinard et al., 2005). This is because the uptake of a metal may depend on the presence of another metal in the pyrite structure, e.g., more Au can be dissolved in As-bearing than As-barren pyrite (Kusebauch et al., 2019; Reich et al., 2005). This is also because pyrite records the conditions in which it precipitates, i.e., the physicochemical fluid parameters that include temperature, pH, redox, and the availability of complex-forming ligands (Deditius et al., 2014; Huston et al., 1995; Keith et al., 2016b; Revan et al., 2014). Pyrite may also record the chemical modifications of the fluid induced by an increased fluid/rock ratio or phase separation (Keith et al., 2016b; Roman et al., 2019; Tardani et al., 2017; Wohlgemuth-Ueberwasser et al., 2015). Partitioning coefficients have seldom been proposed for pyrite (Kusebauch et al., 2019, 2018), possibly in part because equilibrium conditions are rarely attained in hydrothermal systems. An additional difficulty when studying pyrite from high-grade

mineralization is that early precipitated pyrite may be destabilized and/or modified by subsequent fluid circulation (Fougerouse et al., 2016; Xing et al., 2019). Long-lived hydrothermal systems may be essential for concentrating Au, for example, and processes such as metamorphic upgrading, zone refining, or multi-stage events are thus likely frequent (Meffre et al., 2016; Wagner et al., 2007). In such conditions, it might be difficult to "decipher" the chemistry of pyrite

This contribution introduces a methodology to facilitate the use of pyrite chemistry, using the example of the Chibougamau area, Abitibi Subprovince, Québec. The introduced method compares pyrite from the Cu-Au porphyry systems of the Chibougamau area to a "background" signal recorded by pyrite from regional weakly mineralized sedimentary and volcanic environments, i.e., rocks that contain up to 30% pyrite but minor amounts (ppb to ppm levels) of base and precious, such as Au, Ag, Cu and Zn. This study also focuses on pyrite located in a distal position to orebodies, ~100 m away, and on pyrite from weakly mineralized rocks that record a simple (single stage) hydrothermal history.

## 2. Geological setting and sampling

### 2.1. Regional Geology

This study was carried out in the Chibougamau area as this region contains a variety of mineralizing systems, such as VMS and porphyry deposits, as well as a diversity of pyrite-bearing lithologies including sedimentary units, felsic to mafic intrusive and extrusive magmatic rocks. These rocks have mostly been metamorphosed into a greenschist facies, as have most rocks of the Abitibi Subprovince (Faure, 2015; Jolly, 1974).

The Chibougamau area is located in the northeastern corner of the gold-endowed Neoarchean Abitibi Subprovince, which is the largest continuous greenstone belt of the Canadian Shield (Goodwin and Ridler, 1970). Most magmatic activity (synvolcanic period) occurred from > 2790 to ~2710 Ma, and deformation and minor magmatic activity (syntectonic period) occurred from 2701 to 2690 Ma (Leclerc et al., 2017). The synvolcanic period consists of two main volcanic cycles that produced abundant mafic lava flows as well as intermediate to felsic extrusions and volcanoclastic deposits of the Roy Group (Picard and Piboule, 1986). The Roy Group is itself topped by clastic sedimentary rocks of

the Opémisca Group, a ~2700 Ma Timiskaming-style basin that formed during the syntectonic period (David et al., 2007; Leclerc et al., 2012) **(Figure 1)**.

Several intrusions formed during the synvolcanic period including tonalite-trondhjemite-granodiorite (TTG) plutons and the ~2728 Ma (Mortensen, 1993) Lac Doré Complex (LDC), which is a layered complex dominated by anorthosite units that is coeval with volcanic cycle 1 (Allard, 1976) (**Figure 1**). The Chibougamau pluton is a tonalite-trondhjemite-diorite intrusion (TTD) (Mathieu and Racicot, 2019), that was mostly emplaced between 2718–2715 Ma (Krogh, 1982; Pilote et al., 1997) during volcanic cycle 2. The Cummings complex formed during the same period and consists of three ultramafic to mafic sills intruded at the contact between the Bruneau and Blondeau formations (Roberge and Venture sills) and within the Blondeau Formation (Bourbeau sill, ~2717 Ma) (Mortensen, 1993).

The syntectonic period, on the other hand, is dominated by sedimentary units (Opémisca Group), small to intermediate volume granodiorite intrusions, shoshonitic volcanism and large-volume sanukitoid plutons (Frarey and Krogh, 1986; Mortensen, 1993). For a more detailed and recent review of the stratigraphy of the Chibougamau area, the reader is referred to the work of Leclerc et al. (2017).

### 2.2. Sampling of Cu-Au porphyry systems

The Chibougamau pluton is genetically related to the Cu-Au porphyry deposits (Guha et al., 1990; Magnan et al., 1995; Pilote, 2006; Pilote et al., 1998b, 1998a, 1995, 1994, 1993) of the historical mining camp (Central Camp; **Figure 1**), which is the main economic magmatic-hydrothermal system in the Chibougamau area. The Kokko, the Queylus, and the Bruno samples are from Central Camp and nearby porphyry systems (**Table 1**).

The Kokko sample comes from the Central Camp Cu-Au porphyry deposit. The mineralization formed at 2715.2 ± 0.7 based on the dating of intermineral dikes (Pilote, 2006). These deposits may correspond to the deeper portion of a porphyry system (Mathieu and Racicot, 2019), i.e., they may be related to magmatic fluids undiluted by sea water and groundwater. The Kokko sample is located 600 m west of the old Kokko Creek open pit and contains 10% pyrite disseminated in sericitized LDC anorthosite (**Table 1**).

The Queylus sample originates from the main stripping of the Queylus project, a hydrothermal breccia located in an intrusive phase of the Chibougamau pluton (**Figure 1**). The sample contains 30% pyrite disseminated in a sericitized, carbonatized, and silicified brecciated tonalite. The timing of this mineralization is not fully resolved; it may be contemporaneous with the ~2715 Ma Central Camp Cu-Au porphyry system or be related to a late intrusive phase (2705–2701 Ma) of the Chibougamau pluton (David et al., 2011; McNicoll et al., 2008).

The Bruno sample is from a site located next to the main entrance of the old Bruneau mine. The area was mined for Cu, Au, and Ag in the late 1960s. The mineralization consists of veins of chalcopyrite, pyrite, pyrrhotite, and magnetite, and it may be genetically related to the Central Camp system (Duquette, 1966). The Bruno sample contains 15% pyrite disseminated in a mafic volcanoclastic horizon (**Table 1**).

### 2.3. Sampling of weakly mineralized area

In addition to Cu-Au mineralization, a variety of weakly mineralized settings has been sampled. The sampled mineralization corresponds to synvolcanic (seawater-derived fluids circulating within submarine volcanic rocks), syn-sedimentary (diagenetic pyrite), and syntectonic systems (metamorphic and other fluids circulating in < 2700 Ma rocks) (**Table 1**).

The SUL-Vx samples originate from volcanic rocks (volcanic cycles 1 and 2) modified by seawater. The sampled sulfides likely formed on the seafloor (volcanogenic system), as indicated by the inter-pillow sulfides and mineralized cherty horizons (exhalite) observed in the field. The samples come from the volcanic cycle 1, which consist of the undated, large-volume Obatogamau Formation—mostly basaltic to basalt-andesitic lava flows—and the 2729–2727 Ma (Leclerc et al., 2011; Mortensen, 1993) VMS-bearing Waconichi Formation (Mercier-Langevin et al., 2014), a complex assemblage of differentiated volcanic, volcanoclastic, and sedimentary products (**Figure 1**). Other samples come from the base of volcanic cycle 2, i.e., the 2724 Ma (Davis et al., 2014) Bruneau Formation (mafic to intermediate lava flows).

The SUL-V1 sample, located 100 m northeast of the Bruno sample, comes from pillow basalts and contains 5% inter-pillow pyrrhotite ± pyrite. The other samples are basalts that

contain 5% thin-grained pyrite and pyrrhotite (SUL-V2), 15% coarse-grained pyrite (SUL-V3), 3% euhedral pyrite (SUL-V4), and 25% disseminated pyrite (SUL-V5). Additional samples are intermediate to felsic volcanoclastic rocks having 5% pyrite ± pyrrhotite (SUL-V7) and 30% thin- to coarse-grained disseminated pyrite (SUL-V8) (**Table 1**). Sample SUL-V6 comes from a cherty horizon (possibly exhalite) intercalated between basalt lava flows, and this sample contains 5% disseminated pyrrhotite.

Other samples (SUL-Sx) originate from the volcanoclastic and sedimentary rocks of < 2721 Ma (Leclerc et al., 2012) Blondeau Formation (assemblage of felsic extrusions, volcanoclastic and sedimentary products) (**Figure 1**). This formation contains abundant sulfides (commonly > 10–30 vol%) that likely formed in shallow anoxic basins (Archer, 1983; Tait, 1987). The studied samples come from black shale having quartz-carbonate veins that enclose > 50% spongy and euhedral pyrite (samples SUL-S12 and SUL-S13). The SUL-S11 sample contains clasts that are mostly of andesitic composition, as well as 60% nodular pyrite (**Table 1**).

The final two samples (SUL-Tx) contain sulfides formed during the syntectonic period (**Table 1**). SUL-T10 contains 5% euhedral pyrite disseminated in a clastic sedimentary rock of the Bordeleau Formation (**Figure 1**). SUL-T9 comes from the Richardson stripping, a gold showing that belongs to Tarku Resources (Lafrance, 2018). The SUL-T9 sample contains 3% pyrite disseminated in a mafic sill of the Cummings complex.

The studied samples have mostly been metamorphosed into a greenschist facies. The exceptions are samples SUL-V6 and SUL-V5 that have been metamorphosed to upper greenschist–lower amphibolite facies by contact metamorphism (SUL-V6) or burial along the Barlow Fault (SUL-V5) (**Figure 1**).

## 3. Methodology

### 3.1. Analysis

The samples were imaged using a conventional petrographic microscope equipped with an Olympus camera. Additional imaging was performed using the scanning electron microscope (SEM) Zeiss Sigma 300VP of IOS Services Géoscientifiques Inc., Chicoutimi, Québec. Semi-quantitative energy dispersive X-ray spectroscopy (EDS) chemical mapping

(**Figure 2a**) and backscattered imaging (**Figure 2b**) were performed. The EDS detector is an Oxford Ultim-Max 170 $mm^2$, and each pixel (1.77 to 3.53 µm in size, depending on the map) was analyzed for 200 µs. Individual chemical maps were processed using the Aztec 4.0 software and were then combined to produce false color images using ImageJ 1.52a software (**Figure 2a**).

Quantitative laser ablation inductively coupled plasma mass spectrometry (LA-ICP-MS) analyses were carried out on polished thin sections at LabMaTer (UQAC). These *in-situ* analyses were run using a RESOlution ArF-193nm excimer laser ablation system (Australian Scientific Instrument) equipped with a double-volume cell S-155 (Laurin Technics) coupled to an Agilent 7900 ICP-MS. The parameters used for these analyses were a beam size of 75 µm, a laser frequency of 20 Hz, a dwell time of 5 ms for each element and an energy density of 3 $J/cm^2$. Pyrite and reference materials were analyzed using spots (20 s acquisition time), lines (10 µm/s stage speed), and maps (beam size of 15 µm, scan speed of 10 µm/s) after measuring the gas blank for 20 s.

For most elements, calibration was performed using the UQAC-FeS-1 reference material, which is an artificial sulfide produced at UQAC (Savard et al., 2018) based on a modified technique developed at Kiel University (Garbe-Schönberg and Müller, 2014). For Ca, Zr, and Al, calibration relied on the USGS reference material GSE-1g, which is a fused-basaltic glass containing ~10% Fe and doped with ~500 ppm of each trace element (Jochum et al., 2005). MASS-1 (USGS) (Wilson et al., 2002) was used as quality control reference material. Data quality was also monitored using the UQAC-FeS-5 reference material and a massive sulfide reference material: CCU-1e, a copper concentrate (Canadian Certified Reference Materials Project - CCRMP). Pressed pellets were produced from CCRMP powdered reference material using a similar technique for the production of UQAC-FeS-1. It was presumed that the concentrations reported on the certificates of analysis provided by the CCRMP were not affected by the recrushing procedure that involves 60 minutes of crushing in a Planetary Micro Mill (Pulverisette 7, Fritsch) to reduce the powder to a submicron particle size (Garbe-Schönberg and Müller, 2014). The results are in good agreement with working values (see Supplemental material). The RSD (relative standard deviation) are < 5% for the trace elements of interest and for the UQAC-FeS-1 reference material (see Supplemental material for the bulk of RSD values).

### 3.2. Data processing

The line and spot data were reduced using the LADR 0.6.6.0 software (http://norris.org.au/ladr), and maps were produced using the IOLITE software (Paton et al., 2011). The internal standard $^{57}$Fe and the stoichiometric value 46.55 wt% were used (Webmineral mineralogy database http://webmineral.com). A detection limit value was assigned to undetected elements to remove zeros from the dataset.

Line analyses can be processed using a single integration that encompasses the entire analyzed grain and that includes pyrite and the majority of its inclusions (Wohlgemuth-Ueberwasser et al., 2015). Such an approach provides a bulk chemical composition of the studied sulfide. However, pyrite usually has complex texture. Pyrite may comprise inclusion-rich and inclusion-poor areas (**Figure 3a**), as well as multiple overgrowths that vary in chemical composition. If the ratio between inclusion-poor and inclusion-rich areas, for example, varies from one pyrite to the next, considering only the bulk chemical composition of the mineral may induce a bias. For this reason, two types of integrations are run: 1) single integrations that encompass an entire grain performed on line analyses only (DB1 dataset, $n$ = 84) (**Figure 3b**); and 2) distinct integrations applied to inclusion-rich and inclusion-poor pyrites analyzed using lines and spots (DB2 dataset, $n$ = 238) (see Supplementary material for the full LA-ICP-MS dataset, including calibration).

LA-ICP-MS analyses cannot be used to distinguish homogeneously distributed inclusions from lattice-bound elements (Wu et al., 2019), but this is not the purpose of this study. Micro- and larger-sized inclusions, however, produce intensity peaks in time-resolved profiles. From these profiles and microscopic observations, the studied pyrites contain a large amount of sulfide, silicate, and Fe-Ti-oxide inclusions (**Figure 3**). Chalcopyrite is observed in most samples, both inside and outside of the pyrite grains. The other sulfides are less abundant and correspond to pyrrhotite, sphalerite, and ± galena. The silicates and oxide inclusions are the main constituent minerals of the rocks hosting the studied pyrite (**Table 2**). The integrations used to produce the DB1 and DB2 datasets encompass variable amounts and types of inclusions and correspond to mixed compositions. To obtain pyrite-only chemical analyses, additional integrations were performed to compile “time-slice datasets” (TSD), following the recommendations of Gourcerol et al. (2018).

The used integrations correspond to 2 s of acquisition (DB3 dataset), during which the beam traveled for 20 µm across the sample (line analyses; **Figure 3**) or drilled a few µm into the pyrite (spot analyses). The advantage of this technique is that pyrite and its inclusions are treated as distinct analyses. Once exported, data with $Al_2O_3$ + $SiO_2$ + MnO + CaO (wt%) > 5 wt% were removed from the dataset to discard silicate analyses. The DB3 dataset (*n* = 2148) contains pyrite analyses mixed with a minor amount of silicates, Fe-Ti-oxides, or sulfides, except for the analyses where Fe/S > 1 (classified as Fe-rich), Cu > 20,000 ppm (chalcopyrite), and Zn > 15,000 ppm (sphalerite) (Supplementary material). The Fe-rich analyses may correspond to pyrrhotite grains (SUL-V1, SUL-V2, SUL-V5, and SUL-V6) or to magnetite inclusions mixed with the hosting pyrite (SUL-V4). However, ablation of pyrite may fractionate the Fe/S ratio and form deposits with ~FeS composition (Gilbert et al., 2014) that may be ablated during line analysis. This induces imprecise S estimates but does not affect Fe values and metallic ratios, and the Fe-rich analyses of trace elements are considered reliable.

### 3.3. Data analysis

The studied pyrites were analyzed for 32 elements, including the internal standard Fe. Some elements, such as S, Al, Si, Ti, Zr, and Ca, were analyzed to monitor silicate, Fe-Ti-oxide, and pyrrhotite inclusions. This study focuses on the distribution of these elements in pyrite: $^{51}$V, $^{53}$Cr, $^{55}$Mn, $^{59}$Co, $^{61}$Ni, $^{65}$Cu, $^{66}$Zn, $^{71}$Ga, $^{75}$As, $^{82}$Se, $^{107}$Ag, $^{111}$Cd, $^{118}$Sn, $^{121}$Sb, $^{126}$Te, $^{138}$Ba, $^{182}$W, $^{197}$Au, $^{202}$Hg, $^{205}$Tl, $^{208}$Pb, and $^{209}$Bi. Three elements (In, Ge, Mo) were not considered due to their low concentration (< detection limit) in the studied pyrites.

The trace element content of the studied pyrites was compared using binary diagrams and median values, as well as principal component analysis (PCA). PCA is a coordinate transformation method used to reduce the dimensionality of a dataset (*n* observations and *m* variables). The method calculates principal components (PC1, PC2, PC3, etc.) and by considering only PC1 and PC2, the dimensionality of the data is reduced from *m* to a few variables. Data were transformed using a natural logarithm to ensure a normal distribution of data and facilitate combining variables. PCA results are presented in a two-dimensional plot. In this plot, elements are distributed as a function of their degree of correlation

(positive or negative) with respect to the components (PC1 and PC2 or PC3) that best explain the variability in the multidimensional dataset.

Analyses were also compared using median values. This median was calculated using the analyses of the DB3 dataset, as follows: 1) analyses identified as Fe-rich, chalcopyrite, and sphalerite were discarded ($n$ = 1898 data left); 2) a median value per sample was calculated; and 3) the median of these individual medians was calculated. The median value (**Table 3**) was used to normalize the samples displayed on multielement diagrams.

## 4. Results

### 4.1. Kokko sample

The Kokko sample from the main Cu-Au porphyry system of the Chibougamau area (Central Camp) will be described in detail as it is the most likely sample to record the signature of undiluted magmatic fluids in the study area. In this sample, pyrite is disseminated in sericitized anorthosite. The host rock is an assemblage of greenschist facies minerals, i.e., epidote, albite, muscovite, and chlorite (**Figure 2a**). Accessory phases include apatite and magnetite. These silicate and oxide minerals are observed as inclusions in pyrite (**Figure 2a, Table 2**). The pyrite of the Kokko sample is a subeuhedral mineral having an inclusion-rich core and an inclusion-poor rim (**Figures 2 and 3a**). The most common sulfide inclusion is chalcopyrite.

*In-situ* line analyses show that chalcopyrite controls the distribution of the economic metals Cu, Au, and Ag (**Figure 3b**). Other elements, such as Co, have an irregular distribution due to oscillatory zoning (discussed further below). Bismuth and Te also display a complex distribution and are more abundant in the inclusion-rich core than in the inclusion-poor rim of pyrite. Bismuth is slightly more abundant in chalcopyrite inclusions than in the inclusion-rich pyrite (**Figure 3b**). The Kokko pyrite is enriched in Cd, Te, Hg, Bi, and depleted in Cr, As, Se, Sb, Ba, and Pb relative to the other sampled pyrites (**Figure 4a**).

Displaying the DB2 dataset on a binary diagram confirms that the inclusion-rich core of pyrite, which was monitored using Si values (**Figure 4c**), is more enriched in Te and Bi than inclusion-poor pyrite (**Figure 4b**). One pyrite grain is off-trend (highest Bi/Te ratio) because it contains Bi-enriched galena inclusions identified by a Bi-Pb correlation $R^2$ of

0.72. Some inclusion-poor pyrites are also off-trend (lowest Bi/Te ratio) because Te not only concentrates in the core of the pyrite but also defines growth zoning in the inclusion-poor and Bi-poor outer rim of pyrite (see next section).

Binary diagrams also show that the DB1 and DB2 datasets have average chemical compositions that are not as useful as the DB3 dataset for unraveling the chemical complexity of the studied pyrites (**Figure 4b**). However, the DB2 dataset, which documents the inclusion-rich and inclusion-poor portions of pyrite, is more representative of the chemical diversity of the studied pyrite than the DB1 dataset.

### 4.2. Pyrite from magmatic, volcanic, and sedimentary environments

The other samples in this study contain mostly greenschist facies silicates and ± Fe-Ti-oxides, which are observed as inclusions in pyrite (**Figure 5; Table 2**). Pyrite observed in silicified zones or quartz-epidote veins (**Figure 5a–d; Figure 6a**) is more inclusion-poor than pyrite disseminated in less altered rocks (**Figure 5e–f; Figure 6b–k**).

Most pyrites resemble those observed in the Kokko sample: they are euhedral minerals with an inclusion-rich core and inclusion-poor rim (**Figure 6d, e, f, i, k**). Some pyrites have inclusion-poor cores with large sulfide inclusions and inclusion-rich rims (**Figure 5e, f**). Other grains contain only a minor amount of large sulfide and silicate inclusions (**Figure 5a–d, Figure 6a, c, g, i**). Portions of the pyrites are lathlike inclusion-rich minerals (**Figure 6b**) and spongy pyrites that correspond to inclusion-rich aggregates of small (~10–50 µm) pyrite grains (**Figure 6c, f, h, j**). The samples having spongy pyrite also contain thinly disseminated small (typically 10 µm) pyrite (**Figure 6g, h, j**). Spongy pyrite usually has an irregular outline, except for sample SUL-S11, where it forms nodular pyrite (**Figure 6h**).

Based on LA-ICP-MS chemical maps, the 2D distribution of most trace elements is controlled by sulfide, oxide, and silicate inclusions (Supplementary material). The main exceptions are As, Co, Ni, Te, and Bi that concentrate either in the core of the pyrite or mimic the growth zoning of the outer rim (**Figure 7**). Chemical mapping also reveals that most pyrites have complex crystallization histories, with an early core overgrown by pyrites having distinct chemistries (**Figure 7a, b**).

The main elements that mimic the growth zoning of pyrite are Co, Ni, and As. Cobalt is enriched in the outer rim of early pyrite (Kokko and SUL-V8) or pyrite overgrowth (SUL-T9; **Figure 7c**). In contrast to Co, enrichment in As and Ni is most pronounced in pyrite hosted by felsic lithology (SUL-V8; **Figure 7**). In the Kokko sample (**Figure 7a**), Te and Se are more abundant in the inclusion-rich core of pyrite, but also mimic the growth zoning of the inclusion-poor outer rim. In other samples, Te is only detected in the core of pyrite. Selenium is undetected (SUL-V8 and SUL-T9) or concentrates in the early core of pyrite (SUL-V4; Supplementary material). Bismuth is also concentrated in the pyrite core, except in SUL-V4 (**Figure 7c**), but it is most abundant in chalcopyrite ± galena inclusions (**Figure 7**). The other elements are controlled by inclusions. The exceptions are Pb, Ag, and Sb of SUL-V8 that concentrate in the pyrite core (Supplementary material).

For most samples, the core and rim of the bulk of the studied pyrites have different chemistries, as shown by examining the line analyses (**Figure 6** and Supplementary material). Inclusion-rich pyrite is enriched in most elements relative to inclusion-poor pyrite. Spongy pyrite also contains more trace elements than euhedral pyrite observed within the same sample (**Figure 6c, f**). Cobalt generally has an irregular distribution because this element mimics growth zoning. Copper is mostly found in chalcopyrite inclusions (**Figure 6i**). Bismuth and Te have a more homogeneous distribution and concentrate in inclusion-rich pyrite. Bismuth and Te are well correlated in spongy and lathlike pyrite (**Figure 6b, j**) and are less correlated in euhedral grains (**Figure 6d**).

Median chemical compositions are calculated using the DB2 dataset to further evaluate the chemical differences between inclusion-rich and inclusion-poor pyrite. Compared to its inclusion-poor counterpart, inclusion-rich pyrite is enriched in trace elements, Bi and Te included (**Figure 8a**). The main exception is Se that is equally abundant in inclusion-rich and inclusion-poor pyrite, except for SUL-V3, SUL-V8, and SUL-T9 (**Figure 8b**).

Comparing pyrite chemistry with the samples' depositional environments highlights additional chemical associations. The samples from magmatic-hydrothermal systems are most enriched in Te (Queylus samples) and Bi-Te (Kokko and Bruno samples) (**Figure 9a**). The Queylus and Kokko pyrites are also depleted in As and Sb relative to the other pyrites, and these elements are most abundant in sedimentary contexts (**Figure 9b**).

Selenium is enriched in the Bruno sample and some Queylus pyrites, but it is also abundant in other contexts and is not discriminant of magmatic-hydrothermal environments (**Figure 9c**). Tungsten and Sn are detected only locally and are slightly more abundant in the Kokko and some Queylus pyrites than in other samples (**Figure 9d**). Tungsten and Sn are, however, poor discriminants of magmatic-hydrothermal contexts due to their low abundance in the studied pyrite. Cobalt and Ni are only enriched in parts of the Queylus pyrites and does not help discriminate magmatic-hydrothermal settings from other environments (**Figure 9e–f**).

PCA reveals Te and Bi as the best discriminant elements of magmatic-hydrothermal contexts (**Figure 10a, c**). Other elements, such as Cr and V, are most abundant in mafic contexts, whereas Mn is abundant in pyrites hosted by felsic rocks, and Cd and Hg are discriminant of sedimentary contexts (**Figure 10b**). The normalized median values of pyrite chemistry on a multi-element diagram (**Figure 11**) reveal that samples from magmatic-hydrothermal systems are characterized by low As, Sb, Cr, Pb, and Ba contents and elevated Te (Queylus sample) and Bi-Te (Kokko and Bruno samples).

## 5. Discussion

In this first section, the texture of pyrite and the distribution of trace elements are discussed before linking trace element content and mineralizing contexts. Those elements best suited for discriminating magmatic-hydrothermal settings from other pyrite-bearing environments are then discussed.

### 5.1. Pyrite texture and chemical heterogeneity

The studied pyrite records complex crystallization histories. Based on petrographic observations, most pyrites have inclusion-rich cores with irregular outlines and inclusion-poor overgrowths. Inclusion-rich, or porous, pyrite is frequent in sedimentary environments where pyrite crystallizes from low-temperature fluids (Cioacă et al., 2014), as is likely the case for the spongy pyrite of samples SUL-S11 and SUL-S12 (**Figure 6h–j**). Inclusion-rich pyrite may also crystallize rapidly from pyrite-supersaturated solutions in a manner analogous to framboid pyrite (Butler and Rickard, 2000). Porous pyrite is rare in epithermal and porphyry deposits, where they form due to low fluid/rock ratios and relatively quick precipitation or as a result of growth under non-equilibrium conditions

(Cioacă et al., 2014). The inclusion-rich pyrite of the Chibougamau area likely crystallized rapidly, which explains its elevated trace element content relative to the inclusion-poor pyrite. Rapid crystal growth under non-equilibrium conditions favors vacancies and lattice defects, favoring the uptake of As, Au, Te—and likely other elements—by pyrite (Keith et al., 2018; Reich et al., 2005).

In contrast, inclusion-poor or massive subeuhedral pyrite has crystallized more slowly, or it has recrystallized either during the hydrothermal event or the subsequent metamorphism. Indeed, recrystallized pyrite tends to lose its inclusions (Huston et al., 1995) and expel its trace elements as micro-inclusions of chalcopyrite or galena, for example (Cioacă et al., 2014). Trace elements may also be released from pyrite and other sulphides during metamorphism (George et al., 2018a; Lockington et al., 2014). Recrystallized pyrite is euhedral because of the great "crystallization force" of pyrite that can push surrounding minerals as the pyrite cube grows (Craig et al., 1998). Recrystallization may have formed the inclusion-poor core of the pyrite of sample SUL-V4. This recrystallization expelled Cu from the structure of the pyrite to form chalcopyrite inclusions that are now located at the contact between the inclusion-rich and inclusion-poor portions of the pyrite (**Figure 5f**). In other samples, the sulfide inclusions likely coarsened during pyrite recrystallization (**Figure 6i**). The patchy distribution of inclusion-rich areas may also be attributed to the recrystallization of fine-grained pyrite aggregates (**Figure 6f**), as observed elsewhere (Cioacă et al., 2014).

However, recrystallization only explains some of the observations. Recrystallization would have had to expel most trace elements from the pyrite structure to form the inclusion-poor and trace element–depleted pyrite observed in the study area (**Figure 8**). Pyrite may indeed lose As and Sb during recrystallization from a porous to massive texture (Wohlgemuth-Ueberwasser et al., 2015). However, pyrite also has a refractory behavior in regard to metamorphism and does not lose its chemical signature (As, Ni, and Co) during recrystallization under conditions of greenschist and amphibolite facies (Craig et al., 1998). Deformation expulses lattice-bound elements from pyrite more effectively than static recrystallization (Craig et al., 1998; Sung et al., 2009); however, the studied pyrites were sampled away from shear zones and did not display evidence of deformation. In addition,

recrystallization is expected to homogenize the distribution of trace elements and would not explain the growth zoning observed in inclusion-poor pyrite (e.g., **Figure 7a**).

Recrystallization may thus be important only in a few pyrites, such as these of sample SUL-V4, in which chalcopyrite inclusions coarsened and collected Cu and Bi (**Figure 7c**). The majority of inclusion-poor pyrites, however, likely crystallized slowly, possibly in pyrite-saturated—but not oversaturated—fluids, as slowly crystallized pyrite tends to be less enriched in most trace elements than rapidly crystallized pyrite (Hazarika et al., 2013; Huston et al., 1995; Large et al., 2007). Therefore, inclusion-rich and inclusion-poor pyrites either record the circulation of a hydrothermal fluid that evolved from a pyrite-supersaturated to pyrite-saturated state, or they record the circulation of different fluids from successive hydrothermal stages or distinct systems. The inclusion-poor outer rim of pyrite tends to be enriched in As, Ni, and ±Co, whereas the core is enriched in various elements (Bi and Te included), depending on the context. This is discussed in the next section (**Figure 7**).

### 5.2. Elements controlled by inclusions

The studied pyrite contains a large number of silicate inclusions from the hosting lithology (**Figures 5 and 6, Table 2**). The elements associated with silicate and oxide inclusions are Ti and Ca (titanite), V and Cr (magnetite), as well as Mn, Ba, and Ga (feldspar and other silicates). Principal component analysis confirms these associations and shows positive correlations between V and Cr, as well as Mn, Ba, and Ca (**Figure 12**).

Tin and W are positively correlated (**Figure 12**), and the chemical maps (LA-ICP-MS) (Supplementary material) illustrate that they are controlled by inclusions. Tungsten, as well as Mo, is enriched in fluids with a granitic source (Blevin et al., 1996); however, the Chibougamau pluton is not sufficiently differentiated (Mathieu and Racicot, 2019) to produce such fluids. Tungsten is not abundant in the study area, but the slight enrichment of W in the pyrites of the Kokko sample (**Figure 9d**) can be interpreted as related to a magmatic fluid. Tin is a potential discriminant of magmatic-hydrothermal systems as it tends to be most soluble in $CO_2$-rich fluids (Kokh et al., 2017) and be least abundant in oxidized systems (Huston et al., 1995). Tin is, however, a poor discriminant of the

magmatic-hydrothermal systems of the Chibougamau area, as it displays a low abundance in most of the studied pyrites (**Figure 9d**).

Other elements are controlled by sulfide inclusions. Pyrrhotite can incorporate Ni and Co (Bowles et al., 2011; Huston et al., 1995), and these elements can redistribute between pyrite and pyrrhotite during metamorphism (Cambel and Jarkovsky, 1966). Pyrrhotite is only observed in a few samples, and coexisting pyrite and pyrrhotite have comparable Ni and Co contents in the study area. Pyrrhotite thus likely exerts limited control on the distribution of trace elements in the studied pyrite.

Sphalerite can incorporate significant amounts of Cd, Ge, and Ga, whereas galena can incorporate Ag, Bi, and Sb (Bowles et al., 2011), and other elements such as Tl (George et al., 2015). In the studied pyrite, only Cd and Sb are ±correlated with Zn and Pb as shown on the PCA. This pattern suggests that the distribution of Cd and Sb is controlled partially by sphalerite and galena inclusions (**Figure 12**). In detail, the Cd-Zn correlation is best expressed in sample SUL-S12, which contains the largest sphalerite inclusions (**Figure 6i**). Galena micro-inclusions also control the distribution of a minor amount of Bi, as observed in the Kokko sample. In the study area, however, galena is not abundant and controls a limited amount of trace elements. Antimony is correlated weakly with Pb and is uncorrelated to Ag, i.e., galena and tetrahedrite micro-inclusions. Most Sb is structurally bound to pyrite.

In the study area, chalcopyrite is the most abundant sulfide after pyrite. Copper, which can substitute for Fe in pyrite (Bowles et al., 2011), concentrates in chalcopyrite in the studied samples. The ubiquitous presence and relatively high abundance of chalcopyrite in the sulfide-bearing rocks of the Chibougamau area are unique in the Abitibi Subprovince; it is a local peculiarity whose metallogenic implications have not been fully resolved.

Chalcopyrite can incorporate Ag (substituting for Cu), and Sn, Zn, and ±Cd (Huston et al., 1995). In the studied pyrite, chalcopyrite concentrates Au and Ag (**Figure 3**). Statistically, Cu correlates with Au, Ag, ±Cd, and ±Se (**Figure 12**). The Se-Cu correlation is weak and only observed in a few samples (**Figures 8b, 9c**). A small amount of Bi is concentrated by chalcopyrite (**Figures 3, 7c**), but most Bi is associated with pyrite (**Figures 3, 6, 7**). Chalcopyrite can incorporate a wide range of elements (George et al., 2018b), but it only

controls a limited amount of trace elements in the study area. A possible explanation is that the weakly mineralized systems considered by this study have not reached a temperature sufficient (> 300 °C) (George et al., 2018b) to induce the precipitation of significant amounts of chalcopyrite (the porphyry systems excepted). Alternatively, Cu, Au, and Se may have been incorporated by coupled substitutions, such as Au-Cu for $Fe^{2+}$ (Chouinard et al., 2005). Selenium, which substitute for S, may also distort the structure of pyrite and facilitate the incorporation of metals such as Cu (Chouinard et al., 2005). These elements may have been structurally bound to pyrite prior metamorphic recrystallization.

In summary, the distribution of Cd, Sb, and ±Bi-Se is weakly controlled by inclusions. The main elements controlled by inclusions are Mn, Ba, Ga, Cr, V, Zn, Pb, Ag, Cu, Au, and possibly Sn and W. The abundance of these elements depends therefore on the distribution and abundance of silicate, oxide, and sulfide inclusions, and the absolute concentration of these elements in pyrite is not discriminant of the magmatic-hydrothermal systems of the Chibougamau area.

The most efficient way to interpret the abundance of such elements is to use ratios; for example, as Au and Ag are mostly controlled by chalcopyrite, the Au and Ag content of the studied pyrites is best compared using Au/Cu and Ag/Cu ratios (**Figure 13a, b**). A part of the Queylus sulfides are enriched in Au relative to the sulfides from other samples, whereas the Kokko sample is as enriched in Ag as the samples from sedimentary environments. As the studied samples are located away from the main orebodies and record only simple hydrothermal processes—there is no evidence of metal-upgrading processes—the studied sulfides likely approximate the Au/Cu and Ag/Cu ratios of the hydrothermal fluids. The fluids of the Queylus area were therefore more Au-rich than those of Central Camp (Kokko sample). This supports the hypothesis that these systems belong to distinct hydrothermal events (see Section 2.2). The Au/Cu and Ag/Cu, however, are not discriminant of the magmatic-hydrothermal systems of the study area.

### 5.3. Elements sensitive to physicochemical parameters

The most common stoichiometric substitution for Fe in pyrite involves Co and Ni, which may form complete solid solutions above 400–600 °C (Bowles et al., 2011). Cobalt- and Ni-rich sulfides are, however, rare as hydrothermal fluids tend to be undersaturated in these

elements. The studied pyrite follows this general trend and contains a low abundance of Co and Ni (**Figure 9e, f**).

Many studies have used Ni and Co as discrimination tools (Bralia et al., 1979; Campbell and Ethier, 1984; Clark et al., 2004; Fleischer, 1955; Loftus-Hills and Solomon, 1967). However, in the studied pyrites, the Co/Ni ratio is not discriminant of synvolcanic or other mineralizing environments (**Figure 9f**) and there is no correlation with the composition of the host rocks (**Figure 10b**), possibly because of low fluid/rock ratios in the study area.

Cobalt enrichments are observed in Cu deposits, due to the higher solubility of Co in high-temperature fluids (Huston et al., 1995). A slight temperature dependence is also reported in VMS, where the pyrite most enriched in Co-Ni precipitates under high-temperature conditions (Keith et al., 2016a). The PCA illustrates a weak correlation between Co and the samples from Cu-Au magmatic-hydrothermal systems (**Figures 10 and 12**). However, only a portion of the Queylus pyrites is characterized by an elevated Co/Ni ratio (**Figure 9f**), and Co and Ni are poor discriminants of the magmatic-hydrothermal systems of the Chibougamau area.

Nickel and Co mimic the growth zoning in the studied pyrites (**Figure 7**). Cobalt shows the most complex spatial distribution, and its concentration in pyrite likely reflects local fluid conditions such as temperature. This sensitivity to local physicochemical parameters explains why Co and Ni are poor discriminants of fluid chemistry and depositional environments in the study area (**Figure 9e, f**).

### 5.4. Elements enriched in sedimentary environments

Thallium and Sb may be incorporated by coupled substitution, such as $Tl^{+} + Sb^{3+}$ for $2Fe^{2+}$ (George et al., 2018a) and Tl may also occur in structural defects in pyrite (George et al., 2019; Huston et al., 1995). Arsenic is either incorporated in pyrite as nanoparticles (Deditius et al., 2011) or substitutes for Fe or S (Deditius et al., 2008; Fleet and Mumin, 1997; Kusebauch et al., 2018). In addition, As distorts the structure of pyrite to enable the incorporation of elements, such as Au, Hg and Tl (Deditius et al., 2014; Deditius and Reich, 2016).

Arsenic has been most intensely studied because of the control that it exerts on the solubility of Au in pyrite (Reich et al., 2005). The studied pyrites plot below the solubility of Au and are precipitated from Au-undersaturated fluids (**Figure 14**). Arsenic and Au are also correlated in some of the pyrites, particularly those hosted by sedimentary rocks (SUL-T10, SUL-S11, SUL-S12, SUL-S13), in which As was more readily available than in other contexts (**Figure 14**). A weak correlation between As and Au is also observed in the Bruno sample ($R^2$ of 0.18; **Figure 14**)—although not in the Kokko or Queylus samples—where Au is mostly controlled by chalcopyrite. In porphyry deposits, pyrite records the Au/As ratio of the magmatic-hydrothermal fluid (Deditius et al., 2014). If this holds true for the Bruno sample, then the magmatic fluid was not particularly Au-enriched relative to the other hydrothermal fluids of the Chibougamau area (**Figure 14**). The As-content of pyrite from the Bruno, Kokko and Queylus samples varies from 1 to 1000 ppm. This suggests that the magmatic fluid, as recorded by the Kokko sample, was As-poor and that its As-content has been increased by fluid-rock interactions, as recorded at the old Bruno mine (Bruno sample).

Arsenic, as well as Sb and Tl, are common in many Au deposits, especially in black shale- and limestone-hosted systems (Barker et al., 2009; Graham et al., 2009; Ingham et al., 2014; Large et al., 2009; Wagner and Jonsson, 2001). In the Chibougamau area, As, Sb, and Tl are most abundant in pyrite hosted by sedimentary rocks (**Figures 9d, 10c**). The studied pyrite is, however, poor in Tl, As, and Sb relative to pyrite compiled from a variety of environments (Abraitis et al., 2004) because sedimentary rock-hosted mineralization are rare in the Chibougamau area. Arsenic is also abundant in the outer rim of some pyrites (**Figure 7b**), possibly because of prolonged fluid circulation, i.e., a high fluid/rock ratio (Xing et al., 2019). Arsenic is thus a poor discriminant of the magmatic-hydrothermal systems of the Chibougamau area.

Cadmium and Hg are known to accumulate in sedimentary environments (Deditius and Reich, 2016; Thomas et al., 2011); this would explain the Cd and Hg enrichment of pyrite hosted by sedimentary rocks in the study area (**Figures 10, 12**). Mercury, as well as Tl, is also reported in low-temperature assemblages observed in VMS (Kristall et al., 2011). Due to the volatile nature of Tl, Cu-porphyry tends to be Tl-poor (Deditius and Reich, 2016),

as observed in the Chibougamau area (**Figure 12**). None of these elements are useful indicators of magmatic fluid input.

### 5.5. Temperature-dependent element (Se)

This study compares high-temperature pyrite from magmatic-hydrothermal systems (i.e., Kokko, Queylus, and Bruno samples) to pyrite from weakly mineralized area that likely formed at lower temperatures. Temperature-dependent elements may thus be used to discriminate the magmatic-hydrothermal systems from the other environments of the Chibougamau area. The best proxy for fluid temperature is Se (Keith et al., 2018, 2016a), which substitute for S in pyrite (Chouinard et al., 2005; Huston et al., 1995). Se abundance in pyrite increases as the temperature of the fluid decreases (Huston et al., 1995; Keith et al., 2018).

However, Se may be sensitive to other parameters. For example, Se is most abundant in oxidized fluids (Ingham et al., 2014) and is thus statistically less abundant in orogenic gold systems (Keith et al., 2018). Copper-porphyry are also Se-poor, possibly because pyrite incorporates little Se at high temperatures (Keith et al., 2018). In VMS systems, Se is abundant in the high-temperature, Cu-rich portion of the system (Genna, 2015; Grant et al., 2018; Maslennikov et al., 2009), and variable Se/S ratios are due to variations in local pH, redox, and fluid composition (Kristall et al., 2011), including the influx of magmatic fluids (Huston et al., 1995; Layton-Matthews et al., 2008; Martin et al., 2009). Despite these complications, Se remains the best indicator of fluid temperature (Keith et al., 2018).

In the study area, Se abundance varies little between pyrites observed in the same sample, and Se is mostly uncorrelated to Cu (**Figures 8b and 9c**). Selenium is also uncorrelated to mineralizing environments and host-rock composition (**Figures 10 and 12**). Selenium may thus be temperature-dependent, and it can be used as a Se-in-pyrite thermometer (Keith et al., 2018). The estimated temperatures span a 500 °C range (**Figure 15**). The Queylus pyrite has Se-poor rim, possibly developed under higher temperature conditions than its Se-rich core (**Figure 15a**). The Kokko sample contains pyrites that may have formed at ~500 °C. This temperature is realistic for post-Archean porphyry systems, in which chalcopyrite precipitates around 400–500 °C (Sillitoe, 2010), and likely applies to the

porphyry systems of the Archean period (magmas may have been different, but processes were likely similar).

The other > 400 °C calculated temperatures are unrealistic for the study area. These pyrites may have lost Se during metamorphism, but this hypothesis is not favored as Se is located in the structure of pyrite and not in inclusions; therefore, Se tends to be insensitive to metamorphic modifications (Huston et al., 1995). In the study area, the samples that were metamorphosed under upper greenschist to lower amphibolite facies conditions are not systematically Se-poor, e.g., sample SUL-V6. A pyrite from sample SUL-V4 also demonstrates that the Se-content of pyrite is insensitive to metamorphism. The core of the SUL-V4 pyrite has recrystallized to expulse silicate inclusions, coarsen chalcopyrite inclusions, and displace Bi (**Figure 7**). This recrystallization was, however, unable to modify the distribution of Se, Te, and Co, that still outline a cubic core overgrown by a Se-Te-Co-poor pyrite.

Alternatively, the Se/S ratio may be sensitive to mineralogical constraints with Se being incorporated by selenide or preferring chalcopyrite over pyrite (Layton-Matthews et al., 2008; Yamamoto et al., 1984). Nonetheless, this hypothesis is not favored either, as Se and Cu are uncorrelated (**Figure 9c**), and selenide inclusions have not been observed in the study area. However, several pyrites enclose pyrrhotite or magnetite inclusions (SUL-V1, SUL-V3, SUL-V4, and SUL-V5). Among these samples, some pyrites contain > 50–100 ppm Se (SUL-V3 and SUL-V4), suggesting a link between Se-rich pyrite, pyrrhotite and systems having the lowest S activity.

The Se-content of pyrite is also likely sensitive to the availability of Se in the fluid. Some pyrites have Se-rich porous cores and Se-poor and inclusion-poor rims: these rims are unlikely to have crystallized at 500 °C (samples SUL-V3 and SUL-T10; **Figure 15b)**. These Se-poor overgrowths may have precipitated from Se-depleted fluids. The pyrites of SUL-S11 may be Se-poor because Se is not abundant in sedimentary environments and not because precipitation occurred at a high temperature. Selenium in pyrite has been previously correlated to changes in the Se/S of the fluids (Huston et al., 1995); therefore, the Se-in-pyrite thermometer may not apply to pyrite precipitated from Se-undersaturated

fluids. This conclusion is similar to that drawn for As-in-pyrite -thermometer that should only be applied to As-rich systems (Xing et al., 2019).

Despite these limitations, a weak correlation between Te abundance and the < 400 °C temperatures estimated using the Se-in-pyrite thermometer is observed (**Figure 15**). Tellurium is also correlated to Cu in most samples (e.g., *R* of 0.52 for the SUL-V3 sample; supplementary material). Tellurium does not fractionate between chalcopyrite and pyrite, except if these minerals precipitate at different temperatures or if recrystallization occurs (Wohlgemuth-Ueberwasser et al., 2015). In the studied samples, Te is enriched in the porous core of pyrite, where most chalcopyrite inclusions are observed, explaining the Te-Cu correlation. Some of these Te-enriched porous pyrites are also Se-poor due to high temperatures (i.e., 300–400 °C) of crystallization.

### 5.6. Magmatic signature (Bi and Te)

Bismuth and Te are enriched in the porphyry systems of the Chibougamau area (**Figures 10, 11, 12**). Tellurium is most systematically enriched in pyrite that precipitated from fluids having a magmatic origin (samples Kokko, Queylus, Bruno), whereas Bi can be less abundant (**Figure 11**). These elements are also most abundant in the inclusion-rich parts of pyrite (**Figure 4b**).

In most deposits, Te is either structurally bound (substitute for S) or occurs as telluride nanoparticles in pyrite (Pals et al., 2003), while Bi generally concentrates in galena or sulfosalt inclusions (Deditius et al., 2011; Huston et al., 1995), such as telluride and Pb-Cu–bearing sulfosalts (Jian et al., 2014). In the studied pyrite, Te is structurally bound to pyrite, while Bi is found in pyrite and in inclusions of galena and chalcopyrite (**Figures 6 and 7**).

The distribution of Bi is best described by ratios such as Bi/Te (**Figure 9a**), Bi/Pb, and Bi/Cu (**Figure 13c, d**). These ratios confirm that the pyrite associated with magmatic-hydrothermal systems is enriched in Bi relative to its Te content (samples Kokko and Bruno) and has elevated Bi/Pb (Kokko and Queylus) or Bi/Cu ratios (Kokko). In summary, absolute Te concentrations, as well as the Bi/Te, Bi/Cu, and Bi/Pb ratios, confirm that the pyrites precipitated in magmatic-hydrothermal systems are Bi- and Te-enriched compared to the other pyrites considered by this study.

It is concluded that Bi and Te are the best discriminant of magmatic-hydrothermal systems in the Chibougamau area. This conclusion can be drawn because the pyrite of the Cu-Au porphyry systems of the Chibougamau area contain more Bi and Te than the pyrite from regional, weakly mineralized, sedimentary and volcanic environments that record a "background" signal.

### 5.7. Applicability of the method to other contexts

The method introduced in this contribution has two components: 1) documenting the trace elements distribution using 2s integrations (DB3 dataset) to evaluate whether pyrite chemistry should be interpreted using absolute concentration (for elements structurally bound to pyrite) or ratios (for elements controlled by inclusions); and 2) comparing the chemistry of pyrite from the mineralizing systems of interest to a "background" signal to identify the most discriminant elements. This procedure can be applied to any mineralizing contexts. This contribution also concludes on the usefulness of Bi and Te in the Chibougamau area. In this section, the usefulness of Bi and Te as discriminant of magmatic fluids in other areas is discussed.

In porphyry deposits, Bi and Te have a magmatic source (Cioacă et al., 2014), and Bi can be abundant in such systems (Sinclair, 2007). The Bi observed in iron-oxide-Cu-Au (IOCG) systems is also of magmatic origin (Williams et al., 2015). Tellurium tends to concentrate in vapor phases (Cooke and McPhail, 2001), and both Bi and Te are most abundant in epithermal systems (Ciobanu et al., 2006; Franchini et al., 2015). Bismuth and Te are thus potential markers of magmatic fluids in magmatic-hydrothermal systems around the World.

Tellurium is soluble in oxidized fluids having a variable pH, low salinity, and high temperature, and its solubility decreases in reduced conditions (Cook et al., 2009; Cooke and McPhail, 2001; Gao et al., 2017; Grundler et al., 2013; Kelley et al., 1998; Scherbarth and Spry, 2006). Thus, the oxidized magmatic fluids involved in most porphyry systems (Sun et al., 2015)—this includes the Cu-Au deposits of Chibougamau (Mathieu and Racicot, 2019)—may concentrate more easily Te than reduced systems. These remarks should be tempered somewhat as Te can also be transported in reduced S-rich or $CO_2$-rich solutions and vapors (Brugger et al., 2012). This process may explain the Au-Bi-Te-W

metal assemblages that are observed in reduced intrusion-related gold systems (RIRGS, not to be mistaken for the abovementioned IRGS), which are hydrothermal systems related to reduced magmas that interacted with sedimentary rocks (Hart, 2007). In addition, Te transportation is favored by high pH conditions, such as these encountered in epithermal systems associated with alkali magma (Gao et al., 2017; Grundler et al., 2013; Smith et al., 2017). Tellurides are also reported in orogenic gold deposits lacking magmatic fluid input and in which fluid immiscibility may have been a primary mechanism of gold precipitation (Neyedley et al., 2017). Tellurium enrichment may thus be reached in a variety of environments.

A similar remark can be made on Bi. Indeed, native Bi and maldonite are stable in reduced conditions. These conditions may occur in several types of deposits, such as skarns, IRGS, and orogenic gold systems (Cook et al., 2009). The Au-Bi-Te metal association, which is found in a variety of deposits (epithermal, orogenic gold, skarn, IRGS, RIRGS, and VMS), has also been explained by the Bi-collector model. This model stipulates that Bi-liquids may precipitate from a fluid and scavenge gold (Cockerton and Tomkins, 2012; Douglas, 2000; Tooth et al., 2011). Bismuth enrichment may thus not systematically be diagnostic of the involvement of magmatic fluid in a mineralizing system.

In VMS systems, however, Bi and Te are markers of magmatic fluid influx (Wohlgemuth-Ueberwasser et al., 2015). In VMS, Bi and Te may also be controlled by temperature, phase separation, and interactions with Bi-rich sediments (Keith et al., 2016b, 2016a). Bismuth is not usually enriched in diagenetic pyrite but can be observed together with Te in nodular pyrite (Thomas et al., 2011). Both Te and Bi can be released during pyrite recrystallization and integrate orogenic gold-mineralizing systems (Large et al., 2009). Bismuth is also an incompatible element and will be enriched in VMS hosted by felsic volcanic rocks relative to VMS hosted by basalts (Wohlgemuth-Ueberwasser et al., 2015) if the fluid/rock ratio is sufficiently high (Sung et al., 2009). In the studied samples from volcanogenic and sedimentary environments, the fluid/rock ratio is low and the pyrite is not enriched in Bi and Te (**Figure 10**). In other contexts, the fluid/rock ratio would have to be evaluated before concluding that Bi and Te have a magmatic origin and are discriminant of porphyry or other magmatic-hydrothermal systems.

In summary, in the Chibougamau area, Bi and Te are only discriminant of porphyry systems because the other pyrite-bearing environments of the study area are not favorable to concentrating of Bi and Te. However, in other contexts, the fluid/rock ratio, the presence of reduced fluids or Bi-liquids should be evaluated before interpreting the elevated Bi-Te content of pyrite as a magmatic fluid signature.

## 6. Conclusions

This study demonstrates that Bi and Te in pyrite are the most discriminant tracers for magmatic fluid influx into the mineralizing systems of the Chibougamau area. In addition, interpreting pyrite chemistry must consider crystallographic constraints before establishing whether absolute concentrations or ratios reliably indicate the source of the hydrothermal fluids. In the study area, Te is structurally bound to pyrite and absolute Te concentration can be used to interpret pyrite chemistry. Bismuth has a more complex distribution: it is controlled by pyrite as well as chalcopyrite and galena inclusions, and ratios (Bi/Pb, Bi/Cu) are required to interpret the Bi-content of pyrite.

This study established that the Bi and Te contents of pyrite in the Chibougamau area are the best indicators of magmatic fluid circulation. This conclusion is derived from the chemistry of pyrite obtained from magmatic-hydrothermal systems, by taking into account crystallographic constraints and by comparing these results to “background” values, i.e., the chemistry of pyrites from weakly mineralized systems of the same area. It is advised to apply such a procedure to other mineralized systems to interpret fluid signatures. Indeed, a variety of processes may concentrate Bi and Te, and elements discriminant of magmatic fluid signature in the Chibougamau area may provide misleading information in other areas.

This study also provides insights into the magmatic-hydrothermal systems of the Chibougamau area. The Kokko sample from Central Camp, i.e., the main Cu-Au porphyry system of the study area, contains pyrite that formed at elevated temperatures (~500 °C) from undiluted Cu-bearing and not particularly Au-enriched magmatic fluids. The Cu deposit of the old Bruno mine (sample Bruno) is located ~5 km from Central Camp and was formed by similar magmatic fluids that interacted with volcanic and possibly sedimentary rocks (higher fluid/rock ratios). The Queylus breccia likely belongs to a

different hydrothermal system active ~15 Ma after the Central Camp Cu-Au porphyry system and is characterized by Au-richer fluids.

**Acknowledgment**

The author is indebted to editor Huayong Chen and to reviewers Manuel Keith, Blandine Gourcerol and an anonymous reviewer, whose comments helped to greatly improve this manuscript. Warm thanks are addressed to P. Houle (MERN) and the summer 2018 mapping team of the Chibougamau transect (Metal Earth project): P. Bedeaux, M. Kieffer, J. Huguet, A. Boucher, A. Brochu, Y.A. Youssoufou, L.P. Perron-Desmeules, M. Bellemare, and M. Desrochers. Many thanks to J. Tremblay, IOS Services Géoscientifiques Inc., who operated the SEM, and to D. Savard and A. Lavoie, who provided technical support during use of the LA-ICP-MS of LabMaTer. The author is indebted to the many collaborators of the Metal Earth project, including R. Sherlock, H. Gibson, B. Lafrance, P.C. Thurston, J. Ayer, D.J. Kontak, P. Bédard, and R. Daigneault. This paper is Metal Earth contribution number MERC-ME-2019-183.

This study was undertaken as part of the Metal Earth project (Laurentian University) investigation of the Chibougamau area, and this research was funded by Canada First Research Excellence Funds and by federal/provincial/industry partners (http://merc.laurentian.ca/research/metal-earth/). This project was also funded by the NSERC (Natural Sciences and Engineering Research Council) Discovery grant to L. Mathieu (reference number RGPIN-2018-06325) and by UQAC new researcher start-up funds.

**Data availability**

The following are available online (data repository): 1) “LA-ICP-MS_maps.pdf” that contains chemical maps of pyrites from the SUL-V4, SUL-V8, SUL-T9, and Kokko samples; 2) “LA-ICP-MS_lines.pdf” that contains the time-resolved profiles for the pyrites of Figures 3 and 6; 3) “LA-ICP-MS_dataset.xlsx” that contains the DB1, DB2, and DB3 datasets, as well as the LA-ICP-MS standards; and 4) “Correlation-coefficients.xlsx” that contains the R values for the DB3 dataset.

**Table captions**

**Table 1:** Sample list and location.

**Table 2:** Main minerals observed as inclusions in pyrite and in the host rock.

**Table 3:** Median chemical composition of the studied pyrites (in ppm)

**Figure captions**

**Figure 1:** Geological map of the Chibougamau area, showing the main volcanic, sedimentary, and intrusive phases. The geological map is modified from the Ministère de l'Énergie et des Ressources Naturelles (MERN), Québec (SIGEOM, 2018). The projection is UTM NAD83 Zone 18N. This map presents the remaining units of the Gilman Formation in light green, i.e., the color of the Bruneau Formation, following the most recent stratigraphic interpretation (Leclerc et al., 2017). The Caopatina Formation is undated and its relationship with the volcanic cycle 2 and the Opémisca Formation is unresolved.

**Figure 2:** SEM (scanning electron microscope) images of pyrites from the Kokko sample. a) False color image obtained by combining EDS (energy dispersive X-ray spectroscopy) semi-quantitative chemical maps (Ca, Al, and Si) using the ImageJ software; and b) electron backscattered image. These images show that pyrite contains chalcopyrite inclusions and entraps silicates from the groundmass (chlorite, epidote, albite, and muscovite in this example). Mineral abbreviations stand for: albite (Ab), apatite (Ap), chalcopyrite (Cpy), chlorite (Chl), epidote (Ep), magnetite (Mag), muscovite (Ms) and pyrite (Py).

**Figure 3:** Pyrite from the Kokko sample. a) Reflected light image of the grain showing its inclusion-rich core and its inclusion-poor outer rim. The red arrow corresponds to the trace of the 73 µm wide laser ablation line shown in (b); b) Time-resolved profiles showing the distribution of $^{57}$Fe, $^{59}$Co, $^{65}$Cu, $^{125}$Te, $^{107}$Ag, $^{197}$Au, and $^{209}$Bi in pyrite. Note the complex distribution of Co that mimics the growth zoning of pyrite, the Bi- and Te-rich inclusion-rich core of the pyrite, and the spatial association between Ag, Au, and Cu (chalcopyrite inclusions). The integration boxes used to reduce LA-ICP-MS data are shown for the DB1, DB2, and DB3 datasets.

**Figure 4:** Chemical composition of the pyrite of the Kokko sample. a) Box plots displaying the DB3 dataset ($n$ = 267) and comparing it to median values (red rectangles) reported by Table 3. Relative to these median values, the Kokko pyrite is enriched in Cd, Te, Hg, and Bi (orange boxes) and depleted in Cr, As, Sb, Ba, and Pb (blue boxes). b) Bi vs Te binary

diagram comparing the chemistry of the Kokko pyrite as documented by the DB1 ($n$ = 10), DB2 ($n$ = 24), and DB3 ($n$ = 267) datasets. c) Bi vs Te binary diagram displaying the DB3 dataset ($n$ = 267) and using Si as a proxy for inclusion-rich pyrite.

**Figure 5:** SEM (scanning electron microscope) images of pyrite from the Queylus (a–b), SUL-S13 (c–d) and SUL-V4 (e–f) samples. (a, c, e) False color images obtained by combining EDS (energy dispersive X-ray spectroscopy) semi-quantitative chemical maps using the ImageJ software. The images show that all the minerals observed in the groundmass of the rocks can be found in inclusions in the pyrite. (b, d, f) Electron backscattered images showing the distribution of silicate, chalcopyrite, and magnetite inclusions in pyrite. Mineral abbreviations stand for: albite (Ab), amphibole (Amp), apatite (Ap), biotite (Bt), carbonate (Carb), chlorite (Chl), chalcopyrite (Cpy), epidote (Ep), magnetite (Mag), muscovite (Ms), pyrite (Py) and quartz (Qz).

**Figure 6:** Pyrites from the Queylus (a), Bruno (b), SUL-V3 (c), SUL-V4 (d), SUL-T9 (e), SUL-V7 (f), SUL-V8 (g), SUL-S11 (h), SUL-S12 (i), SUL-S12 (j), and SUL-S13 (k) samples. The reflected light images show the trace of the 73 µm wide laser ablation line (red arrow) that goes through inclusion-rich (pink lines) and inclusion-poor (green lines) pyrites. The time-resolved profiles show the distribution of $^{57}$Fe, $^{59}$Co, $^{65}$Cu, $^{125}$Te, and $^{209}$Bi in pyrite. The analyzed pyrites are subeuhedral grains with inclusion-rich and inclusion-poor sectors (a, c, d, e, f, g, i, k), inclusion-rich lathlike pyrites (b), and spongy pyrites with irregular (c, f, j) or nodular (h) outlines. Mineral abbreviations stand for: chalcopyrite (Cpy) and sphalerite (Sph).

**Figure 7:** Reflected light images and chemical maps (LA-ICP-MS) of pyrites from the Kokko (a), SUL-V8 (b), SUL-V4 (c), and SUL-T9 (d) samples. The chemical maps are semi-quantitative, and the color bar goes from 0 to the following maximum (max) values (in ppm): 0.7, 35, 2, and 35 (As); 70, 150, 130, and 120 (Co); 25, 35, 20, and 150 (Ni); 1, 0.23, 0.25, and 1 (Te); 4.5, 0.23, 0.6, and 1 (Bi); and 2.3, 1.3, 5, and 5 (Se) for a, b, c, and d, respectively. The analyzed pyrite records complex growth interpreted using pink dashed lines (reflected light images). The Kokko pyrite (a) has an inclusion-rich and Bi-Te-rich core with a Co-rich overgrowth and an outer rim having As, Co, Ni, and Te oscillatory zoning. The SUL-V8 pyrite (b) has an inclusion-free core with two inclusion-bearing and Bi-rich growth zones that become progressively enriched in As, Co, Ni, and Te, and an As-

and Ni-enriched outer rim. The SUL-V4 pyrite (c) has an inclusion-poor core with large Bi-rich chalcopyrite inclusions and an outer zone of Bi-bearing pyrite enriched in silicate inclusions. The upper-left part of the SUL-V4 pyrite is Se-enriched cubic pyrite with a Co-rich rim and a Se-poor overgrowth. The SUL-T9 (d) pyrite has an As-poor core (magmatic pyrite?) with a Co-poor and Te-Bi-bearing overgrowth that turns into a Co-richer overgrowth with an irregular outline, and a Co-As-enriched and Ni-poor outer rim.

**Figure 8**: Bi vs Te (a) and Se vs Cu (b) binary diagrams that display median values calculated from the DB2 dataset and for inclusion-rich and inclusion-poor pyrites ($n$ = 188). These diagrams show that most elements (except Se) are more abundant in inclusion-rich than inclusion-poor pyrite. The color lines connect the median values calculated for inclusion-rich and inclusion-poor pyrite.

**Figure 9:** Bi vs Te (a), As vs Sb (b), Te vs Se (c), W vs Sn (d), Co vs Ni (e), and Co/Ni vs Co+Ni (f) binary diagrams showing the pyrite ($n$ = 1898) of the DB3 dataset. The color code is designed to help the reader compare the chemistry of the pyrites from magmatic-hydrothermal systems (Kokko, Queylus, and Bruno samples) to those formed in other contexts.

**Figure 10:** Results of principal component analysis (PCA) performed using the DB3 dataset ($n$ = 1898) and the elements of interest as variables ($m$ = 22). The diagrams are displayed, from top to bottom, as a function of PC1 and PC2, PC1 and PC3, and PC2 and PC3. The dataset is displayed on binary diagrams using color codes that refer to the depositional environment (a) and the composition of the host rocks (c). The contribution of each variable is shown using circle diagrams (b).

**Figure 11:** Multi-element diagram for sulfide grains (for pyrite, chalcopyrite, and sphalerite analyses; with Fe-rich analyses discarded) of the DB3 dataset ($n$ = 1947), normalized by the median values reported in Table 3. The elements are displayed in order of increasing abundance in the pyrites of the Kokko sample (red line). These pyrites are richer in Bi and Te and poorer in As, Sb, Cr, Pb, Ba, and Sn than the other pyrites considered. The pyrite from the Queylus sample displays the same tendency as the Kokko sample with the exception of Bi. The pyrite from the old Bruneau mine (Bruno sample) and the nearby SUL-V1 sample is also enriched in Te and ±Bi.

**Figure 12:** Zoom on the circle diagrams of Figure 10, obtained by principal component analysis (PCA) of the DB3 dataset (*n* = 1898). The diagrams are displayed as a function of PC1 and PC2, PC1 and PC3, and PC2 and PC3. The color code enhances the main positive correlations between elements.

**Figure 13:** Ag vs Cu (a), Au vs Cu (b), Bi vs Pb (c), and Bi vs Cu (d) binary diagrams showing the pyrites and other sulfides of the DB3 dataset (*n* = 2145). The color code is designed to help the reader compare the chemistry of the pyrites from magmatic-hydrothermal systems (Kokko, Queylus, and Bruno samples) to those formed in other contexts.

**Figure 14:** Diagram of Au solubility in pyrite as a function of As (Reich et al., 2005), displaying the analyses of the DB3 dataset for which Au is detected, i.e., Au > 0.1 ppm, *n* = 831. The samples are from magmatic-hydrothermal systems (a) and other environments (b). The color code (b) emphasizes the samples for which Au and As are correlated; the other samples are displayed in gray.

**Figure 15:** Binary diagram of ln(Te) vs temperature estimated using the Se-in-pyrite thermometer (Keith et al., 2018). The dots and error bars correspond to median and standard deviation, respectively, calculated using the DB3 dataset (*n* = 2145) (a). Two median values are calculated for the Queylus and SUL-V3 samples, in which Se has a bimodal distribution (a). The bottom diagram (b) shows median values calculated using the analyses of the DB2 dataset and for the samples that contain inclusion-rich and inclusion-poor pyrites (*n* = 188).

**Bibliography**

Abraitis, P.K., Pattrick, R.A.D., Vaughan, D.J., 2004. Variations in the compositional, textural and electrical properties of natural pyrite: a review. Int. J. Miner. Process. 74, 41–59.

Allard, G.O., 1976. Doré Lake Complex and its importance to Chibougamau Geology and Metallogeny. MRN report DPV-386, Ministère des Ressources Naturelles: Québec, QC, Canada.

Archer, P., 1983. Interpretation de l'environnement volcano-sédimentaire de la formation de Blondeau dans la section stratigraphique du lac Barlow, Chibougamau. Unpublished Master thesis, Université du Québec à Chicoutimi, Chicoutimi, QC, Canada.

Barker, S.L.L., Hickey, K.A., Cline, J.S., Dipple, G.M., Kilburn, M.R., Vaughan, J.R., Longo, A.A., 2009. Uncloaking invisible gold: use of nanoSIMS to evaluate gold,

trace elements, and sulfur isotopes in pyrite from Carlin-type gold deposits. Econ. Geol. 104, 897–904.

Blevin, P.L., Chappell, B.W., Allen, C.M., 1996. Intrusive metallogenic provinces in eastern Australia based on granite source and composition. Earth Environ. Sci. Trans. R. Soc. Edinburgh 87, 281–290.

Bowles, J.F.W., Howie, R.A., Vaughan, D.J., Zussman, J., 2011. Non-silicates: volume 5A, in: Deer, W.A., Howie, R.A., Zussman, J. (Eds.), Rock-Forming Minerals. Geological Society, London, United-kingdom, p. 920.

Bralia, A., Sabatini, G., Troja, F., 1979. A revaluation of the Co/Ni ratio in pyrite as geochemical tool in ore genesis problems. Miner. Depos. 14, 353–374.

Brugger, J., Etschmann, B.E., Grundler, P. V, Liu, W., Testemale, D., Pring, A., 2012. XAS evidence for the stability of polytellurides in hydrothermal fluids up to 599 C, 800 bar. Am. Mineral. 97, 1519–1522.

Butler, I.B., Rickard, D., 2000. Framboidal pyrite formation via the oxidation of iron (II) monosulfide by hydrogen sulphide. Geochim. Cosmochim. Acta 64, 2665–2672.

Cambel, B., Jarkovsky, J., 1966. The possibility of utilising of the nickel and cobalt in pyrites as indicators of ore genesis. Geol. Sb. 17, 17–34.

Campbell, F.A., Ethier, V.G., 1984. Nickel and cobalt in pyrrhotite and pyrite from the Faro and Sullivan orebodies. Can. Mineral. 22, 503–506.

Chouinard, A., Paquette, J., Williams-Jones, A.E., 2005. Crystallographic controls on trace-element incorporation in auriferous pyrite from the Pascua epithermal high-sulfidation deposit, Chile, Argentina. Can. Mineral. 43, 951–963.

Cimon, J., 1973. Possibility of an Archean porphyry copper in Quebec. Can. Min. J. 94, 1–57.

Cioacă, M.E., Munteanu, M., Qi, L., Costin, G., 2014. Trace element concentrations in porphyry copper deposits from Metaliferi Mountains, Romania: A reconnaissance study. Ore Geol. Rev. 63, 22–39.

Ciobanu, C.L., Cook, N.J., Spry, P.G., 2006. Preface - Special Issue: telluride and selenide minerals in gold deposits, how and why? Mineral. Petrol. 87, 163–169.

Clark, C., Grguric, B., Mumm, A.S., 2004. Genetic implications of pyrite chemistry from the Palaeoproterozoic Olary Domain and overlying Neoproterozoic Adelaidean sequences, northeastern South Australia. Ore Geol. Rev. 25, 237–257.

Cockerton, A.B.D., Tomkins, A.G., 2012. Insights into the liquid bismuth collector model through analysis of the Bi-Au Stormont skarn prospect, northwest Tasmania. Econ. Geol. 107, 667–682.

Cook, N.J., Ciobanu, C.L., Spry, P.G., Voudouris, P., 2009. Understanding gold-(silver)-telluride-(selenide) mineral deposits. Episodes 32, 249–263.

Cooke, D.R., McPhail, D.C., 2001. Epithermal Au-Ag-Te mineralization, Acupan, Baguio district, Philippines: numerical simulations of mineral deposition. Econ. Geol. 96, 109–131.

Craig, J.R., Vokes, F.M., Solberg, T.N., 1998. Pyrite: physical and chemical textures. Miner. Depos. 34, 82–101.

David, J., Davis, D.W., Dion, C., Goutier, J., Legault, M., Roy, P., 2007. Datations U-Pb Effectuées dans la Sous-province de l'Abitibi en 2005-2006. MRN report RP 2007-01; Ministère des Ressources Naturelles: Québec, QC, Canada.

David, J., Vaillancourt, D., Bandyayera, D., Simard, M., Goutier, J., Pilote, P., Dion, C., Barbe, P., 2011. Datations U-Pb Effectuées dans les Sousprovinces d'Ashuanipi, de La Grande, d'Opinaca et d'Abitibi en 2008-2009. MERN report, RP-2010-11; Ministère de l'Énergie et des Ressources Naturelles: Québec, QC, Canada.

Davis, D., Simard, M., Hammouche, H., Bandyayera, D., Goutier, J., Pilote, P., Leclerc, F., Dion, C., 2014. Datations U-Pb Effectuées dans les Provinces du Supérieur et de Churchill en 2011-2012. MERN report RP-2014-05; Ministère de l'Énergie et des Ressources Naturelles: Québec, QC, Canada.

De Souza, S., Dubé, B., McNicoll, V., Dupuis, C., Mercier-Langevin, P., Creaser, R.A., Kjarsgaard, I., 2016. Geology and Hydrothermal Alteration of the World-Class Canadian Malartic Gold Deposit: Genesis of an Archean Stockwork-Disseminated Gold Deposit in the Abitibi Greenstone Belt, Québec. Rev. Econ Geol 19, 263.

Deditius, A.P., Reich, M., 2016. Constraints on the solid solubility of Hg, Tl, and Cd in arsenian pyrite. Am. Mineral. 101, 1451–1459.

Deditius, A.P., Reich, M., Kesler, S.E., Utsunomiya, S., Chryssoulis, S.L., Walshe, J., Ewing, R.C., 2014. The coupled geochemistry of Au and As in pyrite from hydrothermal ore deposits. Geochim. Cosmochim. Acta 140, 644–670.

Deditius, A.P., Utsunomiya, S., Reich, M., Kesler, S.E., Ewing, R.C., Hough, R., Walshe, J., 2011. Trace metal nanoparticles in pyrite. Ore Geol. Rev. 42, 32–46.

Deditius, A.P., Utsunomiya, S., Renock, D., Ewing, R.C., Ramana, C. V, Becker, U., Kesler, S.E., 2008. A proposed new type of arsenian pyrite: Composition, nanostructure and geological significance. Geochim. Cosmochim. Acta 72, 2919–2933.

Douglas, N., 2000. The liquid bismuth collector model: an alternative gold deposition mechanism, in: Geological Society of Australia Abstracts. Geological Society of Australia; 1999, p. 135.

Duquette, G., 1966. Description of showing C-MCK-14. Report GM-25117, Brosnan Chibougamau Mines Ltd., Chibougamau, QC, Canada.

Duuring, P., Cassidy, K.F., Hagemann, S.G., 2007. porphyry style metal deposits in the Archean Yilgarn Craton , Western Australia. Ore Geol. Rev. 32, 157–186. https://doi.org/10.1016/j.oregeorev.2006.11.001

Faure, S., 2015. Relations entre les minéralisations aurifères et les isogrades métamorphiques en Abitibi / Relationship between gold mineralisations and metamorphic isogrades in Abitibi [online]. Consorem project 2013-03, available at: http://www.consorem.ca/rapports_publics.html (accessed on 10th of august 2018).

Fayol, N., Jébrak, M., 2017. Archean sanukitoid gold porphyry deposits: a new

understanding and genetic model from the Lac Bachelor gold deposit, Abitibi, Canada. Econ. Geol. 112, 1913–1936.

Fleet, M.E., Mumin, A.H., 1997. Gold-bearing arsenian pyrite and marcasite and arsenopyrite from Carlin Trend gold deposits and laboratory synthesis. Am. Mineral. 82, 182.

Fleischer, M., 1955. Minor elements in some sulfide minerals. Econ. Geol 50, 1024.

Fougerouse, D., Micklethwaite, S., Tomkins, A.G., Mei, Y., Kilburn, M., Guagliardo, P., Fisher, L.A., Halfpenny, A., Gee, M., Paterson, D., 2016. Gold remobilisation and formation of high grade ore shoots driven by dissolution-reprecipitation replacement and Ni substitution into auriferous arsenopyrite. Geochim. Cosmochim. Acta 178, 143–159.

Franchini, M., McFarlane, C., Maydagan, L., Reich, M., Lentz, D.R., Meinert, L., Bouhier, V., 2015. Trace metals in pyrite and marcasite from the Agua Rica porphyry-high sulfidation epithermal deposit, Catamarca, Argentina: Textural features and metal zoning at the porphyry to epithermal transition. Ore Geol. Rev. 66, 366–387.

Frarey, M.J., Krogh, T.E., 1986. U-Pb zircon ages of late internal plutons of the Abitibi and eastern Wawa subprovinces, Ontario and Quebec, in: Current Research, Part A. Geological Survey of Canada, Paper 86-1A, pp. 43–48.

Galley, A.G., Hannington, M.D., Jonasson, I.R., 2007. Volcanogenic massive sulphide deposits, in: Mineral Deposits of Canada: A Synthesis of Major Deposit-Types, District Metallogeny, the Evolution of Geological Provinces, and Exploration Methods. Geological Association of Canada, Mineral Deposits Division: St. John's, NL, Canada, pp. 141–161.

Gao, S., Xu, H., Li, S., Santosh, M., Zhang, D., Yang, L., Quan, S., 2017. Hydrothermal alteration and ore-forming fluids associated with gold-tellurium mineralization in the Dongping gold deposit, China. Ore Geol. Rev. 80, 166–184.

Garbe-Schönberg, D., Müller, S., 2014. Nano-particulate pressed powder tablets for LA-ICP-MS. J. Anal. At. Spectrom. 29, 990–1000.

Genna, D., 2015. Traceurs géochimiques pour guider l'exploration des SMV le long des tuffites de Matagami. Unpublished PhD thesis, Université du Québec à Chicoutimi, Chicoutimi, QC, Canada.

George, L., Cook, N.J., Ciobanu, C.L., Wade, B.P., 2015. Trace and minor elements in galena: A reconnaissance LA-ICP-MS study. Am. Mineral. 100, 548–569.

George, L.L., Biagioni, C., D'Orazio, M., Cook, N.J., 2018a. Textural and trace element evolution of pyrite during greenschist facies metamorphic recrystallization in the southern Apuan Alps (Tuscany, Italy): influence on the formation of Tl-rich sulfosalt melt. Ore Geol. Rev. 102, 59–105.

George, L.L., Biagioni, C., Lepore, G.O., Lacalamita, M., Agrosì, G., Capitani, G.C., Bonaccorsi, E., D'Acapito, F., 2019. The speciation of thallium in (Tl, Sb, As)-rich pyrite. Ore Geol. Rev. 107, 364–380.

George, L.L., Cook, N.J., Crowe, B.B.P., Ciobanu, C.L., 2018b. Trace elements in hydrothermal chalcopyrite. Mineral. Mag. 82, 59–88.

Gilbert, S.E., Danyushevsky, L. V, Goemann, K., Death, D., 2014. Fractionation of sulphur relative to iron during laser ablation-ICP-MS analyses of sulphide minerals: implications for quantification. J. Anal. At. Spectrom. 29, 1024–1033.

Goodwin, A.M., Ridler, R.H., 1970. The Abitibi orogenic belt, in: Baer, A.J. (Ed.), Symposium on Basins and Geosynclines of the Canadian Shield. Geological Association of Canada: Wininipeg, MB, Canada, 10-15 May, pp. 1–31.

Graham, G.E., Kelley, K.D., Slack, J.F., Koenig, A.E., 2009. Trace elements in Zn-Pb-Ag deposits and related stream sediments, Brooks Range Alaska, with implications for Tl as a pathfinder element. Geochemistry Explor. Environ. Anal. 9, 19–37.

Grant, H.L.J., Hannington, M.D., Petersen, S., Frische, M., Fuchs, S.H., 2018. Constraints on the behavior of trace elements in the actively-forming TAG deposit, Mid-Atlantic Ridge, based on LA-ICP-MS analyses of pyrite. Chem. Geol. 498, 45–71. https://doi.org/https://doi.org/10.1016/j.chemgeo.2018.08.019

Grundler, P. V, Brugger, J., Etschmann, B.E., Helm, L., Liu, W., Spry, P.G., Tian, Y., Testemale, D., Pring, A., 2013. Speciation of aqueous tellurium (IV) in hydrothermal solutions and vapors, and the role of oxidized tellurium species in Te transport and gold deposition. Geochim. Cosmochim. Acta 120, 298–325.

Guha, J., Chown, E., Archambault, G., Barnes, S.-J., Brisson, H., Daigneault, R., Dion, C., Dubé, B., Mueller, W.U., Pilote, P., 1990. Metallogeny in relation to magmatic and structural evolution of an Archean greenstone belt: Chibougamau mining district, in: Hoe, S.E., Robert, F., Groves, D.I. (Eds.), Gold and Base-Metal Mineralization in the Abitibi Subprovince, Canada, with Emphasis on the Québec Segment. The University of Western Australia: Perth, Australia, pp. 121–166.

Guha, J, Lange-Brard, F., Péloquin, S., Tremblay, A., Racicot, D., Bureau, S., 1984. Devlin deposit, a part of an Archean porphyry system?, in: Guha, Jayanta, Chown, E. (Eds.), Chibougamau, Stratigraphy and Mineralization. Canadian Institute of Mining and Metallurgy: Westmount, QC, Canada, pp. 345–356.

Hannington, M.D., de Ronde, C.D.J., Petersen, S., 2005. Sea-floor tectonics and submarine hydrothermal systems, in: Hedenquist, J.W., Thompson, J.F.H., Goldfarb, R.J., Richards, J.P. (Eds.), One Hundredth Anniversary Volume. Society of Economic Geologists, Littelton, Colorado, USA, pp. 111–141.

Hart, C.J.R., 2007. Reduced intrusion-related gold systems. Miner. Depos. Canada A Synth. Major Depos. types, Dist. Metallog. Evol. Geol. Prov. Explor. methods Geol. Assoc. Canada, Miner. Depos. Div. Spec. Publ. 5, 95–112.

Hazarika, P., Mishra, B., Chinnasamy, S.S., Bernhardt, H.-J., 2013. Multi-stage growth and invisible gold distribution in pyrite from the Kundarkocha sediment-hosted gold deposit, eastern India. Ore Geol. Rev. 55, 134–145.

Helt, K.M., Williams-Jones, A.E., Clark, J.R., Wing, B.A., Wares, R.P., 2014. Constraints on the genesis of the Archean oxidized, intrusion-related Canadian Malartic gold deposit, Quebec, Canada. Econ. Geol. 109, 713–735.

Huston, D.L., Sie, S.H., Suter, G.F., Cooke, D.R., Both, R.A., 1995. Trace elements in sulfide minerals from eastern Australian volcanic-hosted massive sulfide deposits; Part I, Proton microprobe analyses of pyrite, chalcopyrite, and sphalerite, and Part II, Selenium levels in pyrite; comparison with delta 34 S values ... Econ. Geol. 90, 1167–1196.

Ingham, E.S., Cook, N.J., Cliff, J., Ciobanu, C.L., Huddleston, A., 2014. A combined chemical, isotopic and microstructural study of pyrite from roll-front uranium deposits, Lake Eyre Basin, South Australia. Geochim. Cosmochim. Acta 125, 440–465.

Jian, W., Lehmann, B., Mao, J., Ye, H., Li, Z., Zhang, J., Zhang, H., Feng, J., Ye, Y., 2014. Telluride and Bi-sulfosalt mineralogy of the Yangzhaiyu gold deposit, Xiaoqinling region, Central China. Can. Mineral. 52, 883–898.

Jochum, K.P., Willbold, M., Raczek, I., Stoll, B., Herwig, K., 2005. Chemical Characterisation of the USGS Reference Glasses GSA 1G, GSC 1G, GSD 1G, GSE 1G, BCR 2G, BHVO 2G and BIR 1G Using EPMA, ID TIMS, ID-ICP-MS and LA-ICP-MS. Geostand. Geoanalytical Res. 29, 285–302.

Jolly, W.T., 1974. Regional metamorphic zonation as an aid in study of Archean terrains: Abitibi region, Ontario. Can. Mineral. 12, 499–508.

Katz, L.R., Kontak, D.J., Dubé, B., McNicoll, V., 2017. The geology, petrology, and geochronology of the Archean Côté Gold large-tonnage, low-grade intrusion-related Au (±Cu) deposit, Swayze greenstone belt, Ontario, Canada. Can. J. Earth Sci. 54, 173–202.

Keith, M., Haase, K.M., Klemd, R., Krumm, S., Strauss, H., 2016a. Systematic variations of trace element and sulfur isotope compositions in pyrite with stratigraphic depth in the Skouriotissa volcanic-hosted massive sulfide deposit, Troodos ophiolite, Cyprus. Chem. Geol. 423, 7–18.

Keith, M., Hackel, F., Haase, K.M., Schwarz-Schampera, U., Klemd, R., 2016b. Trace element systematics of pyrite from submarine hydrothermal vents. Ore Geol. Rev. 72, 728–745.

Keith, M., Smith, D.J., Jenkin, G.R.T., Holwell, D.A., Dye, M.D., 2018. A review of Te and Se systematics in hydrothermal pyrite from precious metal deposits: Insights into ore-forming processes. Ore Geol. Rev. 96, 269–282.

Kelley, K.D., Romberger, S.B., Beaty, D.W., Pontius, J.A., Snee, L.W., Stein, H.J., Thompson, T.B., 1998. Geochemical and geochronological constraints on the genesis of Au-Te deposits at Cripple Creek, Colorado. Econ. Geol. 93, 981–1012.

Kokh, M.A., Akinfiev, N.N., Pokrovski, G.S., Salvi, S., Guillaume, D., 2017. The role of carbon dioxide in the transport and fractionation of metals by geological fluids. Geochim. Cosmochim. Acta 197, 433–466.

Kristall, B., Nielsen, D., Hannington, M.D., Kelley, D.S., Delaney, J.R., 2011. Chemical microenvironments within sulfide structures from the Mothra Hydrothermal Field: Evidence from high-resolution zoning of trace elements. Chem. Geol. 290, 12–30.

Krogh, T.E., 1982. Improved accuracy of U-Pb zircon ages by the creation of more concordant systems using an air abrasion technique. Geochim. Cosmochim. Acta 46, 637–649.

Kusebauch, C., Gleeson, S.A., Oelze, M., 2019. Coupled partitioning of Au and As into pyrite controls formation of giant Au deposits. Sci. Adv. 5, eaav5891.

Kusebauch, C., Oelze, M., Gleeson, S.A., 2018. Partitioning of arsenic between hydrothermal fluid and pyrite during experimental siderite replacement. Chem. Geol. 500, 136–147.

Lafrance, B., 2018. Travaux d'exploration 2016-2017, projet Richardson, Chibougamau, Québec. Report GM-70535, Tarku Resources Ltd., Saskatoon, SK, Canada.

Large, R.R., Danyushevsky, L., Hollit, C., Maslennikov, V., Meffre, S., Gilbert, S., Bull, S., Scott, R., Emsbo, P., Thomas, H., 2009. Gold and trace element zonation in pyrite using a laser imaging technique: implications for the timing of gold in orogenic and Carlin-style sediment-hosted deposits. Econ. Geol. 104, 635–668.

Large, R.R., Maslennikov, V. V, Robert, F. ois, Danyushevsky, L. V, Chang, Z., 2007. Multistage sedimentary and metamorphic origin of pyrite and gold in the giant Sukhoi Log deposit, Lena gold province, Russia. Econ. Geol. 102, 1233–1267.

Layton-Matthews, D., Peter, J.M., Scott, S.D., Leybourne, M.I., 2008. Distribution, mineralogy, and geochemistry of selenium in felsic volcanic-hosted massive sulfide deposits of the Finlayson Lake district, Yukon Territory, Canada. Econ. Geol. 103, 61–88.

Leclerc, F., Bédard, J.H., Harris, L.B., McNicoll, V.J., Goulet, N., Roy, P., Houle, P., 2011. Tholeiitic to calc-alkaline cyclic volcanism in the Roy Group, Chibougamau area, Abitibi Greenstone Belt—revised stratigraphy and implications for VHMS exploration. Can. J. Earth Sci. 48, 661–694.

Leclerc, F., Harris, L.B., Bédard, J.H., van Breemen, O., Goulet, N., 2012. Structural and Stratigraphic Controls on Magmatic, Volcanogenic, and Shear Zone-Hosted Mineralization in the Chapais-Chibougamau Mining Camp, Northeastern Abitibi, Canada. Econ. Geol. 107, 963–989.

Leclerc, F., Roy, P., Pilote, P., Bédard, J.H., Harris, L.B., McNicoll, V.J., Breemen, O. van, David, J., Goulet, N., 2017. Géologie de la Région de Chibougamau. MERN report RG 2015-03, Ministère de l'Énergie et des Ressources Naturelles: Québec, QC, Canada.

Lockington, J.A., Cook, N.J., Ciobanu, C.L., 2014. Trace and minor elements in sphalerite from metamorphosed sulphide deposits. Mineral. Petrol. 108, 873–890.

Loftus-Hills, G., Solomon, M., 1967. Cobalt, nickel and selenium in sulphides as indicators of ore genesis. Miner. Depos. 2, 228–242.

Magnan, M., Daigneault, R., Robert, F., Pilote, P., 1995. Intrusion-related Au-Cu-Ag sulfide rich veins in the Archean Doré Lake Complex, Chibougamau, Québec, in: Precambrian '95, International Conference on Tectonics and Metallogeny of Early/Mid Proterozoic Orogenic Belts, Montreal, Canada, August 28 - September 1.

p. 296.

Martin, H., Moyen, J.-F., Rapp, R., 2009. The sanukitoid series: magmatism at the Archaean-Proterozoic transition. Earth Environ. Sci. Trans. R. Soc. Edinburgh 100, 15–33.

Maslennikov, V. V, Maslennikova, S.P., Large, R.R., Danyushevsky, L. V, 2009. Study of trace element zonation in vent chimneys from the Silurian Yaman-Kasy volcanic-hosted massive sulfide deposit (Southern Urals, Russia) using laser ablation-inductively coupled plasma mass spectrometry (LA-ICPMS). Econ. Geol. 104, 1111–1141.

Mathieu, L., Racicot, D., 2019. Petrogenetic Study of the Multiphase Chibougamau Pluton: Archaean Magmas Associated with Cu-Au Magmato-Hydrothermal Systems. Minerals 9, 174.

McNicoll, V., Dubé, B., Goutier, J., Mercier-Langevin, P., Dion, C., Monecke, T., Ross, P.-S.–, Thurston, P., Pilote, P., Bédard, J., Leclerc, F., Bécu, V., Percival, J., Legault, M., Gibson, H., Ayer, J., 2008. Nouvelles datations U-Pb dans le Cadre du Projet ICG-3 Abitibi/Plan Cuivre : Incidences pour l'Interprétation Géologique et l'Exploration des Métaux Usuels. MRN report DV-2008-06; Ministère des Ressources Naturelles: Québec, QC, Canada.

Meffre, S., Large, R.R., Steadman, J.A., Gregory, D.D., Stepanov, A.S., Kamenetsky, V.S., Ehrig, K., Scott, R.J., 2016. Multi-stage enrichment processes for large gold-bearing ore deposits. Ore Geol. Rev. 76, 268–279.

Mercier-Langevin, P., Hannington, M.D., Dubé, B., Bécu, V., 2011. The gold content of volcanogenic massive sulfide deposits. Miner. Depos. 46, 509–539.

Mercier-Langevin, P., Lafrance, B., Bécu, V., Dubé, B., Kjarsgaard, I., Guha, J., 2014. The Lemoine auriferous volcanogenic massive sulfide deposit, Chibougamau camp, Abitibi greenstone belt, Quebec, Canada: Geology and genesis. Econ. Geol. 109, 231–269.

Mortensen, J.K., 1993. U–Pb geochronology of the eastern Abitibi subprovince. Part 1: Chibougamau–Matagami–Joutel region. Can. J. Earth Sci. 30, 11–28.

Neyedley, K., Hanley, J.J., Fayek, M., Kontak, D.J., 2017. Textural, fluid inclusion, and stable oxygen isotope constraints on vein formation and gold precipitation at the 007 deposit, Rice Lake Greenstone Belt, Bissett, Manitoba, Canada. Econ. Geol. 112, 629–660.

Pals, D.W., Spry, P.G., Chryssoulis, S., 2003. Invisible gold and tellurium in arsenic-rich pyrite from the Emperor gold deposit, Fiji: implications for gold distribution and deposition. Econ. Geol. 98, 479–493.

Paton, C., Hellstrom, J., Paul, B., Woodhead, J., Hergt, J., 2011. Iolite: Freeware for the visualisation and processing of mass spectrometric data. J. Anal. At. Spectrom. 26, 2508–2518.

Phillips, G.N., Powell, R., 2010. Formation of gold deposits: a metamorphic devolatilization model. J. Metamorph. Geol. 28, 689–718.

Picard, C., Piboule, M., 1986. Pétrologie des roches volcaniques du sillon de roches vertes archéennes de Matagami-Chibougamau à l'ouest de Chapais (Abitibi est, Québec). 1. Le groupe basal de Roy. Can. J. Earth Sci. 23, 561–578.

Pilote, P., 2006. Le camp minier de Chibougamau et le parautochtone grenvillien : Métallogénie, métamorphisme et aspects structuraux, in: Livret-Guide d'Excursion B1. Joined anual meeting, Geological Association of Canada – Mineralogical Association of Canada (GAC-MAC), Montréal, QC, Canada, 12-14 May 2006, p. 138.

Pilote, P., Allard, G.O., Bellevance, Y., Blais, A., Brisson, H., Chown, E., Daigneault, R., de Corta, H., Dion, C., Gervais, D., Girard, P.A., Girard, R., Guha, J., Kikham, R., Larouche, V., Lavallière, G., Maltais, G., Morin, R., Mueller, W., Robert, F., Schmitt, L., Simard, M., Sinclair, W.D., 1998a. Géologie et métallogénie du district minier de Chapais-Chibougamau : Nouvelle vision du potentiel de découverte. MRN report DV-98-03, Ministère des Ressources Naturelles: Québec, QC, Canada.

Pilote, P., Cimon, J., Dion, C., Kirkham, R., Robert, F., Sinclair, W.D., Daigneault, R., 1993. Les Gisements de Type Cu-Au Porphyrique de la Région de Chibougamau. MRN report DP 93-02; Ministère des Ressources Naturelles: Québec, QC, Canada.

Pilote, P., Cimon, J., Dion, C., Kirkham, R.V., Robert, F., Sinclair, W.D., Daigneault, R., 1994. Les minéralisations de type porphyrique de la région de Chibougamau : Connections possibles avec les gisements filoniens de la région de lac Doré?, in: Congrès Annuel de l'Association Professionnel Des Géologues et Géophysiciens Du Québec (APGGQ), Val-d'Or, QC, Canada, 1-3 May. p. 100.

Pilote, P., Dion, C., Joanisse, A., David, J., Machado, N., Kirkham, R. V, Robert, F., 1997. Géochronologie des minéralisations d'affiliation magmatique de l'Abitibi, secteurs Chibougamau et de Troilus-Frotet: implications géotectoniques, in: Programme et Résumés, Séminaire d'information Sur La Recherche Géologique. MRN report, DV-97-03; Ministère des Ressources Naturelles: Québec, QC, Canada, p. 47.

Pilote, P., Dion, C., Morin, R., 1996. Géologie et évolution métallogénique de la région de Chibougamau : des gîtes de type Cu-Au-Mo porphyriques aux gisements filoniens mésothermaux aurifères. MRN report MB-96-14; Ministère des Ressources Naturelles: Québec, QC, Canada.

Pilote, P., Kirkham, R.V., Robert, F., Sinclair, W.D., Daigneault, R., Magnan, M., 1995. Développement d'un District à Minéralisation de type Cu-Au (Mo) Porphyrique dans la Région de Chibougamau et Implications Métallogéniques. MRN report DV 95-04; Ministère des Ressources Naturelles: Québec, QC, Canada.

Pilote, P., Robert, F., Kirkham, R., Daigneault, R., Sinclair, W.D., 1998b. Minéralisation de type porphyrique et filonienne dans le Complexe du lac Doré—le secteur du lac Clark et de l'île Merrill., in: Pilote, P. (Ed.), Géologie et Métallogénie Du District Minier de Chapais-Chibougamau : Nouvelle Vision Du Potentiel de Découverte. MRN report DV 98-03, Ministère des Ressources Naturelles: Québec, QC, Canada, pp. 71–90.

Reich, M., Kesler, S.E., Utsunomiya, S., Palenik, C.S., Chryssoulis, S.L., Ewing, R.C.,

2005. Solubility of gold in arsenian pyrite. Geochim. Cosmochim. Acta 69, 2781–2796.

Revan, M.K., Genc, Y., Maslennikov, V. V, Maslennikova, S.P., Large, R.R., Danyushevsky, L. V, 2014. Mineralogy and trace-element geochemistry of sulfide minerals in hydrothermal chimneys from the Upper-Cretaceous VMS deposits of the eastern Pontide orogenic belt (NE Turkey). Ore Geol. Rev. 63, 129–149.

Robert, F., 2001. Syenite-associated disseminated gold deposits in the Abitibi greenstone belt, Canada. Miner. Depos. 36, 503–516.

Robert, F., Poulsen, K.H., 1999. Felsic-intrusion-related Gold Deposits: Diversity and its Significance.

Roberts, F.I., 1982. Trace element chemistry of pyrite: A useful guide to the occurrence of sulfide base metal mineralization. J. Geochemical Explor. 17, 49–62.

Roman, N., Reich, M., Leisen, M., Morata, D., Barra, F., Deditius, A.P., 2019. Geochemical and micro-textural fingerprints of boiling in pyrite. Geochim. Cosmochim. Acta 246, 60–85.

Savard, D., Bouchard-Boivin, B., Barnes, S.-J., Garbe-Schönberg, D., 2018. UQAC-FeS: A new series of base metal sulfide quality control reference material for LA-ICP-MS analysis, in: 10th International Conference on the Analysis of Geological and Environmental Materials, Sydney, Australia, 8-13 July.

Scherbarth, N.L., Spry, P.G., 2006. Mineralogical, Petrological, Stable Isotope, and Fluid Inclusion Characteristics of the Tuvatu Gold-Silver Telluride Deposit, Fiji: Comparisons with the Emperor Deposit. Econ. Geol. 101, 135–158. https://doi.org/10.2113/gsecongeo.101.1.135

SIGEOM, 2018. Système d'information géominière du Québec - SIGEOM [WWW Document]. Ministère l'Énergie des Ressources Nat. URL http://sigeom.mines.gouv.qc.ca (accessed 8.20.08).

Sillitoe, R.H., 2010. Porphyry copper systems. Econ. Geol. 105, 3–41.

Sinclair, W.D., 2007. Porphyry deposits, in: Mineral Deposits of Canada: A Synthesis of Major Deposit-Types, District Metallogeny, the Evolution of Geological Provinces, and Exploration Methods. Geological Association of Canada, Mineral Deposits Division: St. John's, NL, Canada, pp. 223–243.

Smith, D.J., Naden, J., Jenkin, G.R.T., Keith, M., 2017. Hydrothermal alteration and fluid pH in alkaline-hosted epithermal systems. Ore Geol. Rev. 89, 772–779. https://doi.org/https://doi.org/10.1016/j.oregeorev.2017.06.028

Sun, W., Huang, R., Li, H., Hu, Y., Zhang, C., Sun, S., Zhang, L., Ding, X., Li, C., Zartman, R.E., 2015. Porphyry deposits and oxidized magmas. Ore Geol. Rev. 65, 97–131.

Sung, Y.-H., Brugger, J., Ciobanu, C.L., Pring, ASkinner, W., Nugus, M., 2009. Invisible gold in arsenian pyrite and arsenopyrite from a multistage Archaean gold deposit: Sunrise Dam, Eastern Goldfields Province, Western Australia. Miner. Depos. 44, 765–791.

Tait, L., 1987. The character of organic matter and the partitioning of trace and rare earth elements in black shales; Blondaeu Formation, Chibougamau, Québec. Unpublished Master thesis, Université du Québec à Chicoutimi, Chicoutimi, QC, Canada.

Tardani, D., Reich, M., Deditius, A.P., Chryssoulis, S., Sanchez-Alfaro, P., Wrage, J., Roberts, M.P., 2017. Copper-arsenic decoupling in an active geothermal system: A link between pyrite and fluid composition. Geochim. Cosmochim. Acta 204, 179–204.

Thomas, H. V, Large, R.R., Bull, S.W., Maslennikov, V., Berry, R.F., Fraser, R., Froud, S., Moye, R., 2011. Pyrite and pyrrhotite textures and composition in sediments, laminated quartz veins, and reefs at Bendigo gold mine, Australia: insights for ore genesis. Econ. Geol. 106, 1–31.

Tooth, B., Ciobanu, C.L., Green, L., O'Neill, B., Brugger, J., 2011. Bi-melt formation and gold scavenging from hydrothermal fluids: An experimental study. Geochim. Cosmochim. Acta 75, 5423–5443.

Wagner, T., Jonsson, E., 2001. Mineralogy of sulfosalt-rich vein-type ores, Boliden massive sulfide deposit, Skellefte district, northern Sweden. Can. Mineral. 39, 855–872.

Wagner, T., Klemd, R., Wenzel, T., Mattsson, B., 2007. Gold upgrading in metamorphosed massive sulfide ore deposits: Direct evidence from laser-ablation–inductively coupled plasma–mass spectrometry analysis of invisible gold. Geology 35, 775–778.

Williams, M.R., Holwell, D.A., Lilly, R.M., Case, G.N.D., McDonald, I., 2015. Mineralogical and fluid characteristics of the fluorite-rich Monakoff and E1 Cu–Au deposits, Cloncurry region, Queensland, Australia: Implications for regional F–Ba-rich IOCG mineralisation. Ore Geol. Rev. 64, 103–127.

Wilson, S.A., Ridley, W.I., Koenig, A.E., 2002. Development of sulfide calibration standards for the laser ablation inductively-coupled plasma mass spectrometry technique. J. Anal. At. Spectrom. 17, 406–409.

Wohlgemuth-Ueberwasser, C.C., Viljoen, F., Petersen, S., Vorster, C., 2015. Distribution and solubility limits of trace elements in hydrothermal black smoker sulfides: An in-situ LA-ICP-MS study. Geochim. Cosmochim. Acta 159, 16–41.

Wu, Y.-F., Fougerouse, D., Evans, K., Reddy, S.M., Saxey, D.W., Guagliardo, P., Li, J.-W., 2019. Gold, arsenic, and copper zoning in pyrite: A record of fluid chemistry and growth kinetics. Geology 47, 641–644.

Xing, Y., Brugger, J., Tomkins, A., Shvarov, Y., 2019. Arsenic evolution as a tool for understanding formation of pyritic gold ores. Geology 47, 335–338.

Yamamoto, M., Kase, K., Tsutsumi, M., 1984. Fractionation of sulfur isotopes and selenium between coexisting sulfide minerals from the Besshi deposit, Central Shikoku, Japan. Miner. Depos. 19, 237–242.

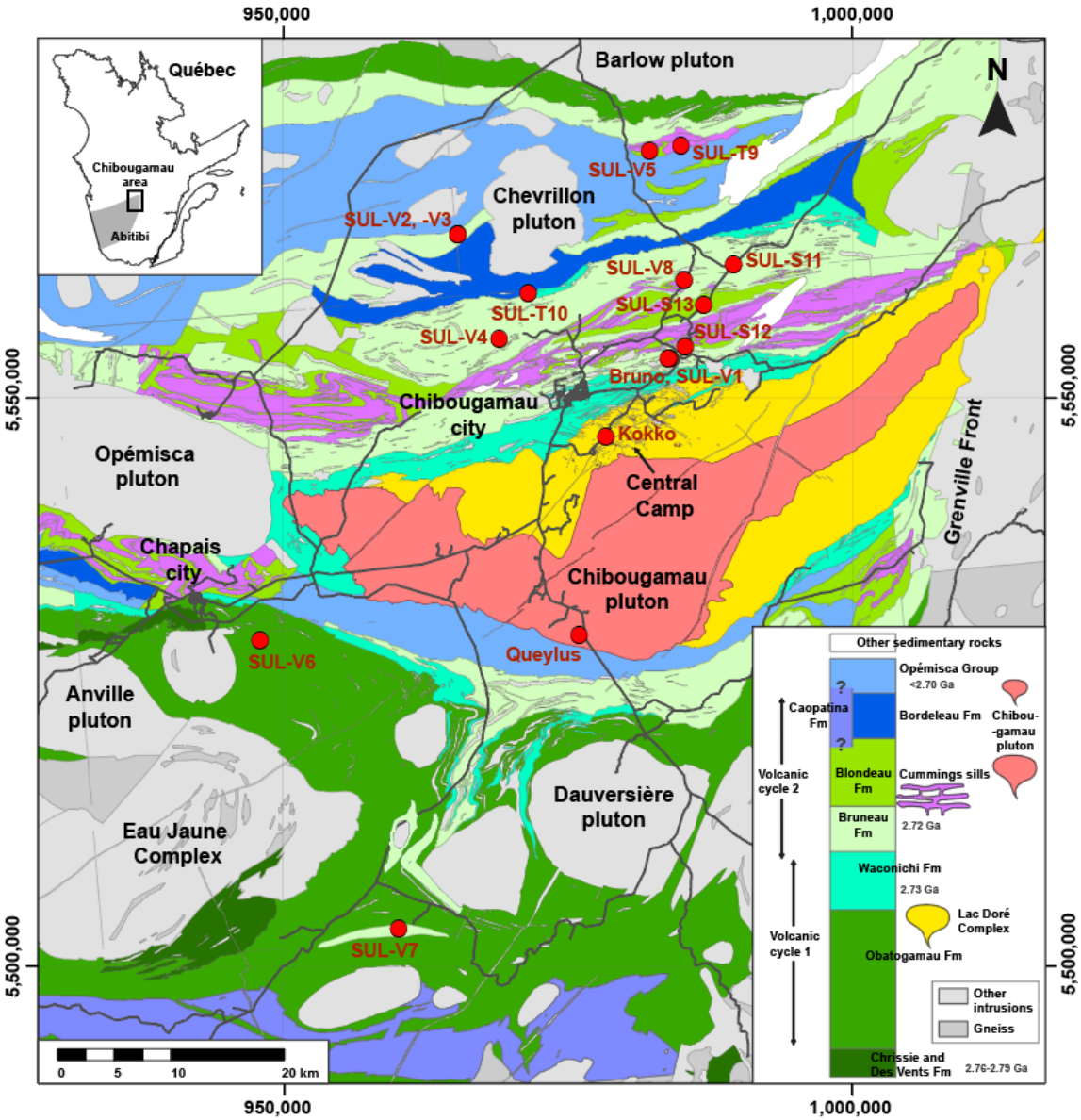


**Figure 1:** Geological map of the Chibougamau area, showing the main volcanic, sedimentary, and intrusive phases. The geological map is modified from the Ministère de l'Énergie et des Ressources Naturelles (MERN), Québec (SIGEOM 2018). The projection is UTM NAD83 Zone 18N. This map presents the remaining units of the Gilman Formation in light green, i.e., the color of the Bruneau Formation, following the most recent stratigraphic interpretation (Leclerc et al. 2017). The Caopatina Formation is undated and its relationship with the volcanic cycle 2 and the Opémisca Formation is unresolved.

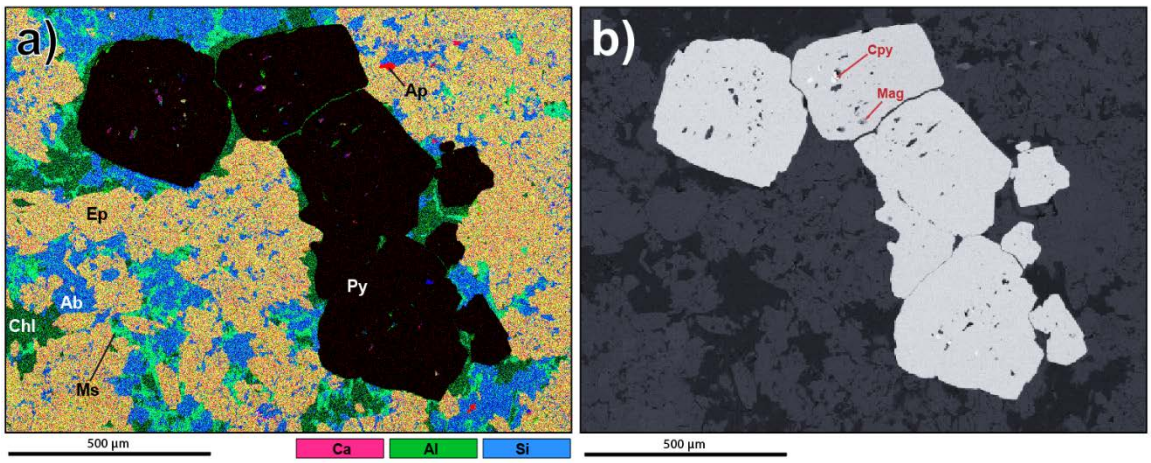


**Figure 2:** SEM (scanning electron microscope) images of pyrites from the Kokko sample. a) False color image obtained by combining EDS (energy dispersive X-ray spectroscopy) semi-quantitative chemical maps (Ca, Al, and Si) using the ImageJ software; and b) electron backscattered image. These images show that pyrite contains chalcopyrite inclusions and entraps silicates from the groundmass (chlorite, epidote, albite, and muscovite in this example). Mineral abbreviations as reported in the literature (Whitney and Evans 2010).

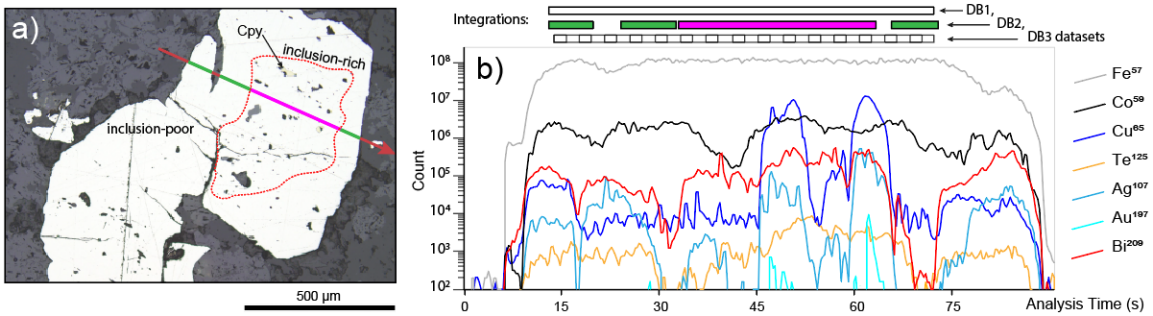


**Figure 3:** Pyrite from the Kokko sample. a) Reflected light image of the grain showing its inclusion-rich core and its inclusion-poor outer rim. The red arrow corresponds to the trace of the 73 µm wide laser ablation line shown in (b); b) Time-resolved profiles showing the distribution of $^{57}$Fe, $^{59}$Co, $^{65}$Cu, $^{125}$Te, $^{107}$Ag, $^{197}$Au, and $^{209}$Bi in pyrite. Note the complex distribution of Co that mimics the growth zoning of pyrite, the Bi- and Te-rich inclusion-rich core of the pyrite, and the spatial association between Ag, Au, and Cu (chalcopyrite inclusions). The integration boxes used to reduce LA-ICP-MS data are shown for the DB1, DB2, and DB3 datasets.

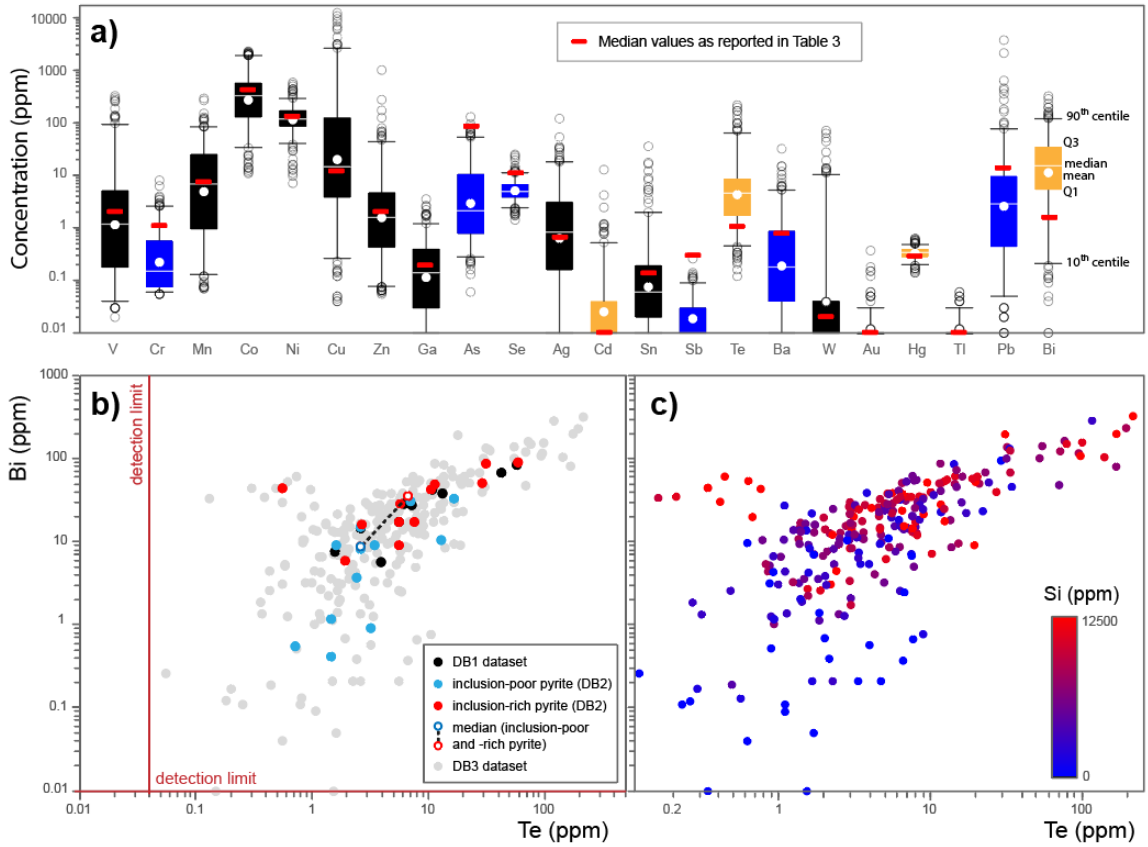


**Figure 4:** Chemical composition of the pyrites of the Kokko sample. a) Box plots displaying the DB3 dataset (*n* = 267) and comparing it to median values (red rectangles) reported by Table 3. Relative to these median values, the Kokko pyrites are enriched in Cd, Te, Hg, and Bi (orange boxes) and depleted in Cr, As, Sb, Ba, and Pb (blue boxes). b) Bi vs Te binary diagram comparing the chemistry of the Kokko pyrites as documented by the DB1 (*n* = 10), DB2 (*n* = 24), and DB3 (*n* = 267) datasets. c) Bi vs Te binary diagram displaying the DB3 dataset (*n* = 267) and using Si as a proxy for inclusion-rich pyrites.

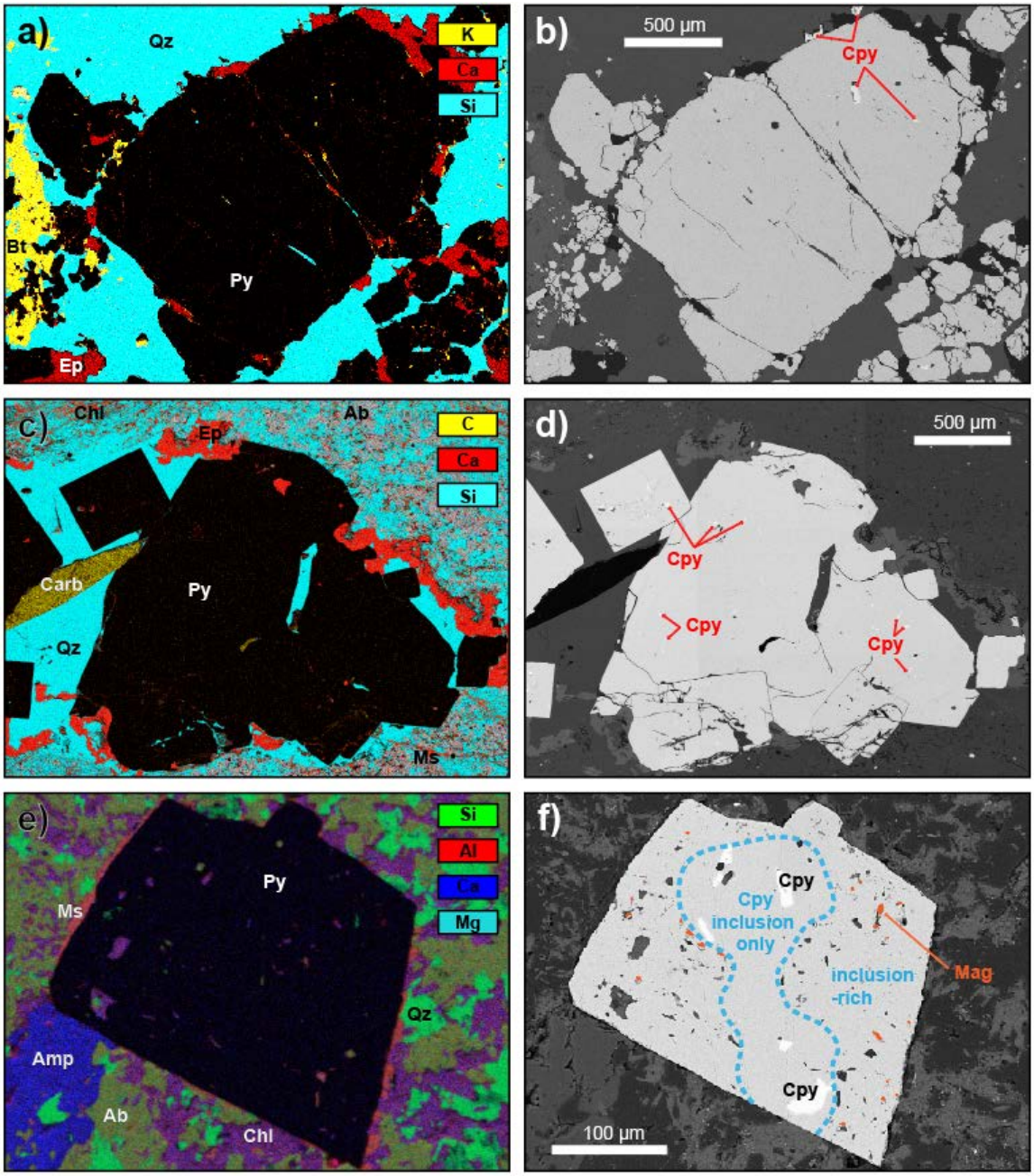


**Figure 5:** SEM (scanning electron microscope) images of pyrites from the Queylus (a–b), SUL-S13 (c–d) and SUL-V4 (e–f) samples. (a, c, e) False color images obtained by combining EDS (energy dispersive X-ray spectroscopy) semi-quantitative chemical maps using the ImageJ software. The images show that all the minerals observed in the groundmass of the rocks can be found in inclusions in the pyrite. (b, d, f) Electron backscattered images showing the distribution of silicate, chalcopyrite, and magnetite

inclusions in pyrite. Mineral abbreviations as reported in the literature (Whitney and Evans 2010).

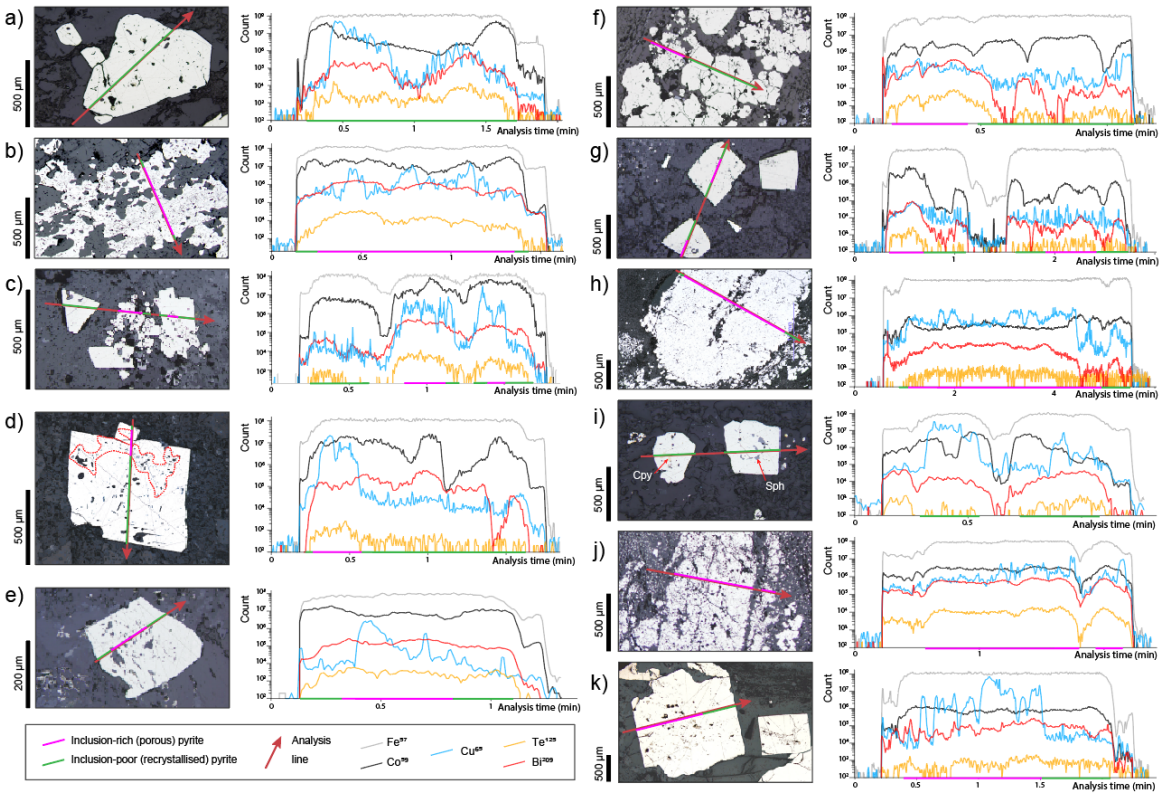


**Figure 6:** Pyrites from the Queylus (a), Bruno (b), SUL-V3 (c), SUL-V4 (d), SUL-T9 (e), SUL-V7 (f), SUL-V8 (g), SUL-S11 (h), SUL-S12 (i), SUL-S12 (j), and SUL-S13 (k) samples. The reflected light images show the trace of the 73 µm wide laser ablation line (red arrow) that goes through inclusion-rich (pink lines) and inclusion-poor (green lines) pyrites. The time-resolved profiles show the distribution of $^{57}$Fe, $^{59}$Co, $^{65}$Cu, $^{125}$Te, and $^{209}$Bi in pyrite. The analyzed pyrites are subeuhedral grains with inclusion-rich and inclusion-poor sectors (a, c, d, e, f, g, i, k), inclusion-rich lathlike pyrites (b), and spongy pyrites with irregular (c, f, j) or nodular (h) outlines. Mineral abbreviations as reported in the literature (Whitney and Evans 2010).

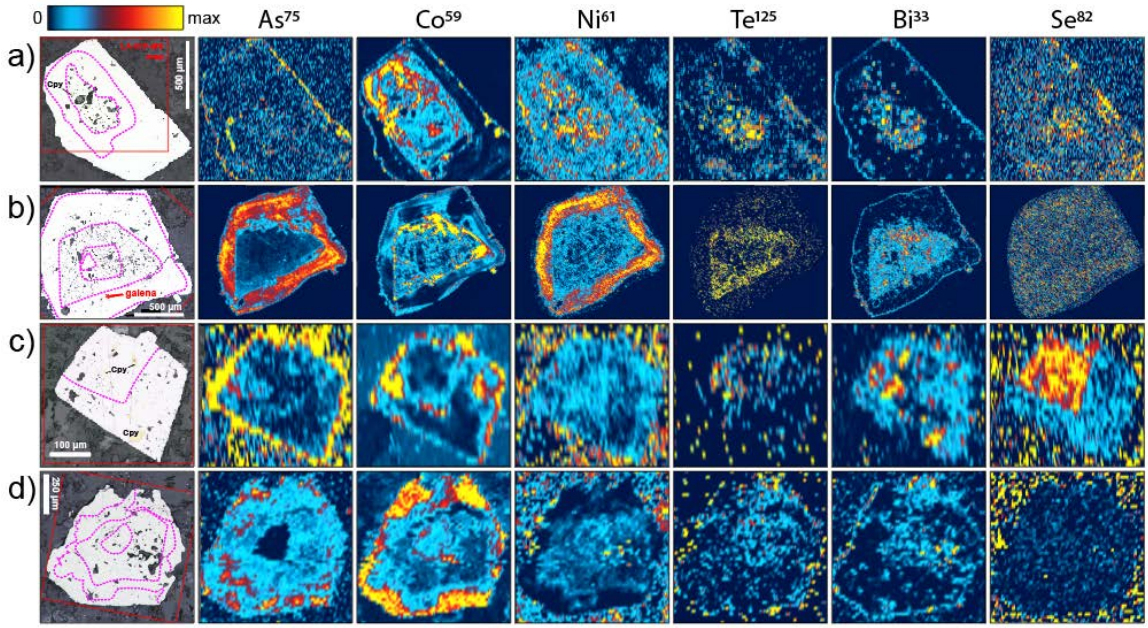


**Figure 7:** Reflected light images and chemical maps (LA-ICP-MS) of pyrites from the Kokko (a), SUL-V8 (b), SUL-V4 (c), and SUL-T9 (d) samples. The chemical maps are semi-quantitative, and the color bar goes from 0 to the following maximum (max) values (in ppm): 0.7, 35, 2, and 35 (As); 70, 150, 130, and 120 (Co); 25, 35, 20, and 150 (Ni); 1, 0.23, 0.25, and 1 (Te); 4.5, 0.23, 0.6, and 1 (Bi); and 2.3, 1.3, 5, and 5 (Se) for a, b, c, and d, respectively. The analyzed pyrites record complex growth interpreted using pink dashed lines (reflected light images). The Kokko pyrite (a) has an inclusion-rich and Bi-Te-rich core with a Co-rich overgrowth and an outer rim having As, Co, Ni, and Te oscillatory zoning. The SUL-V8 pyrite (b) has an inclusion-free core with two inclusion-bearing and Bi-rich growth zones that become progressively enriched in As, Co, Ni, and Te, and an As- and Ni-enriched outer rim. The SUL-V4 pyrite (c) has an inclusion-poor core with large Bi-rich chalcopyrite inclusions and an outer zone of Bi-bearing pyrite enriched in silicate inclusions. The upper-left part of the SUL-V4 pyrite is Se-enriched cubic pyrite with a Co-rich rim and a Se-poor overgrowth. The SUL-T9 (d) pyrite has an As-poor core (magmatic pyrite?) with a Co-poor and Te-Bi-bearing overgrowth that turns into a Co-richer overgrowth with an irregular outline, and a Co-As-enriched and Ni-poor outer rim.

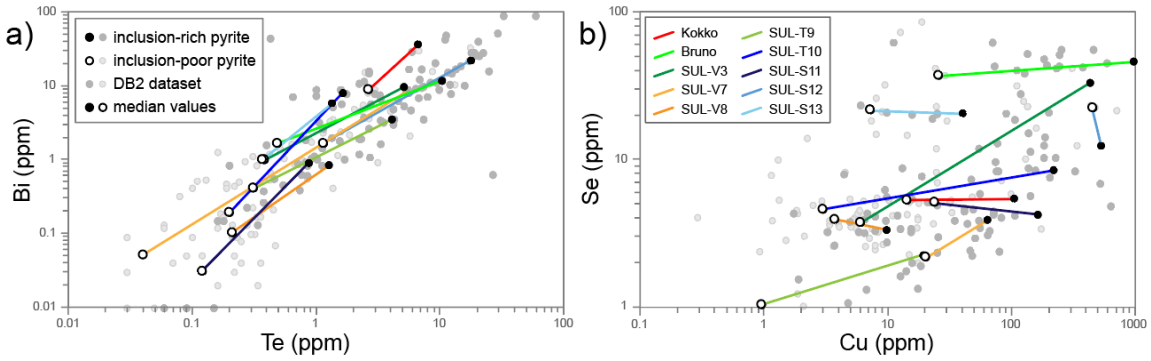


**Figure 8**: Bi vs Te (a) and Se vs Cu (b) binary diagrams that display median values calculated from the DB2 dataset and for inclusion-rich and inclusion-poor pyrites (*n* = 188). These diagrams show that most elements (except Se) are more abundant in inclusion-rich than inclusion-poor pyrites. The color lines connect the median values calculated for inclusion-rich and inclusion-poor pyrites of the displayed samples.

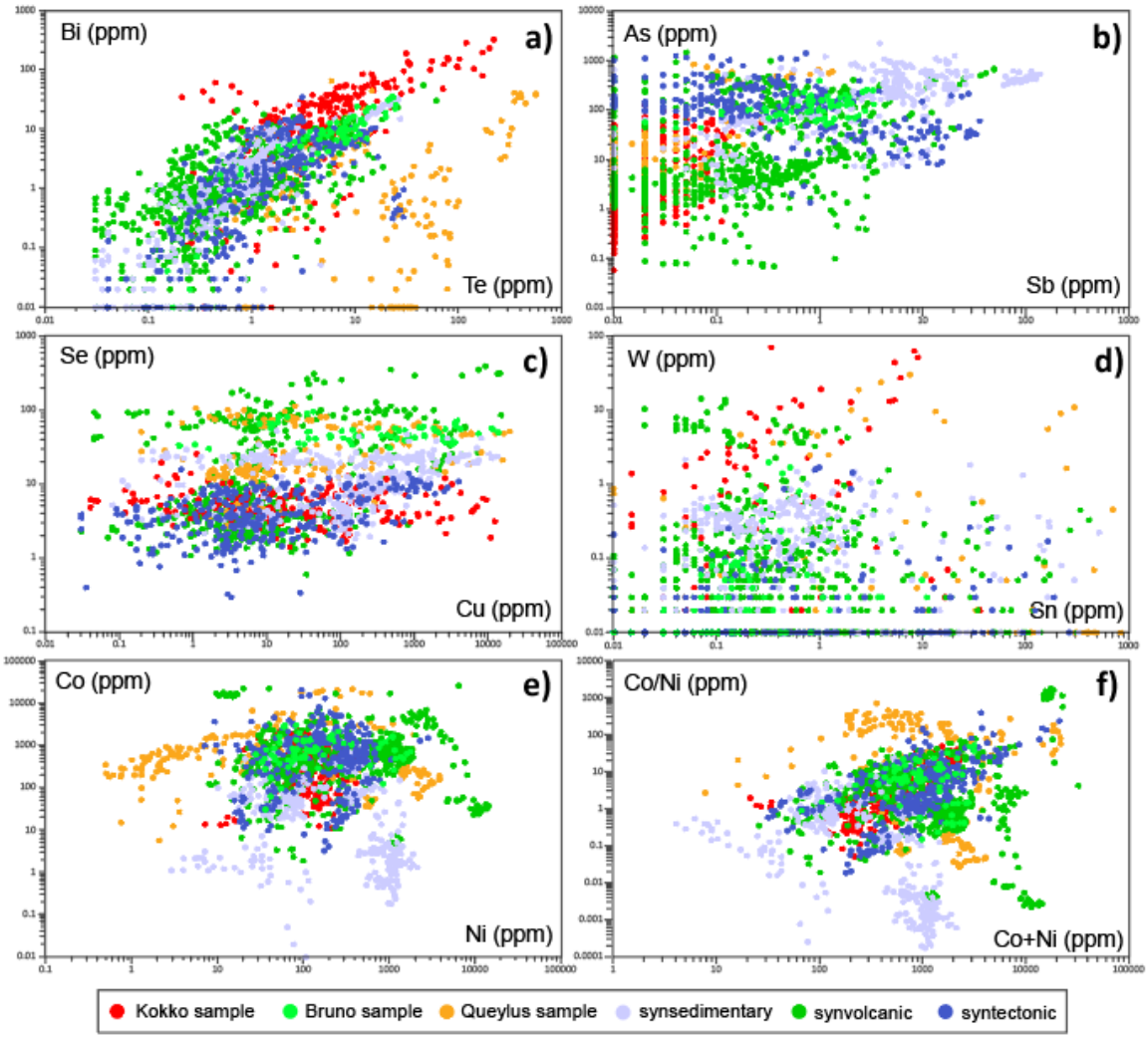


**Figure 9:** Bi vs Te (a), W vs Sn (b), Te vs Se (c), As vs Sb (d), Co vs Ni (e), and Co/Ni vs Co+Ni (f) binary diagrams showing the pyrites (*n* = 1898) of the DB3 dataset. The color code is designed to help the reader compare the chemistry of the pyrites from magmatic-hydrothermal systems (Kokko, Queylus, and Bruno samples) to those formed in other contexts.

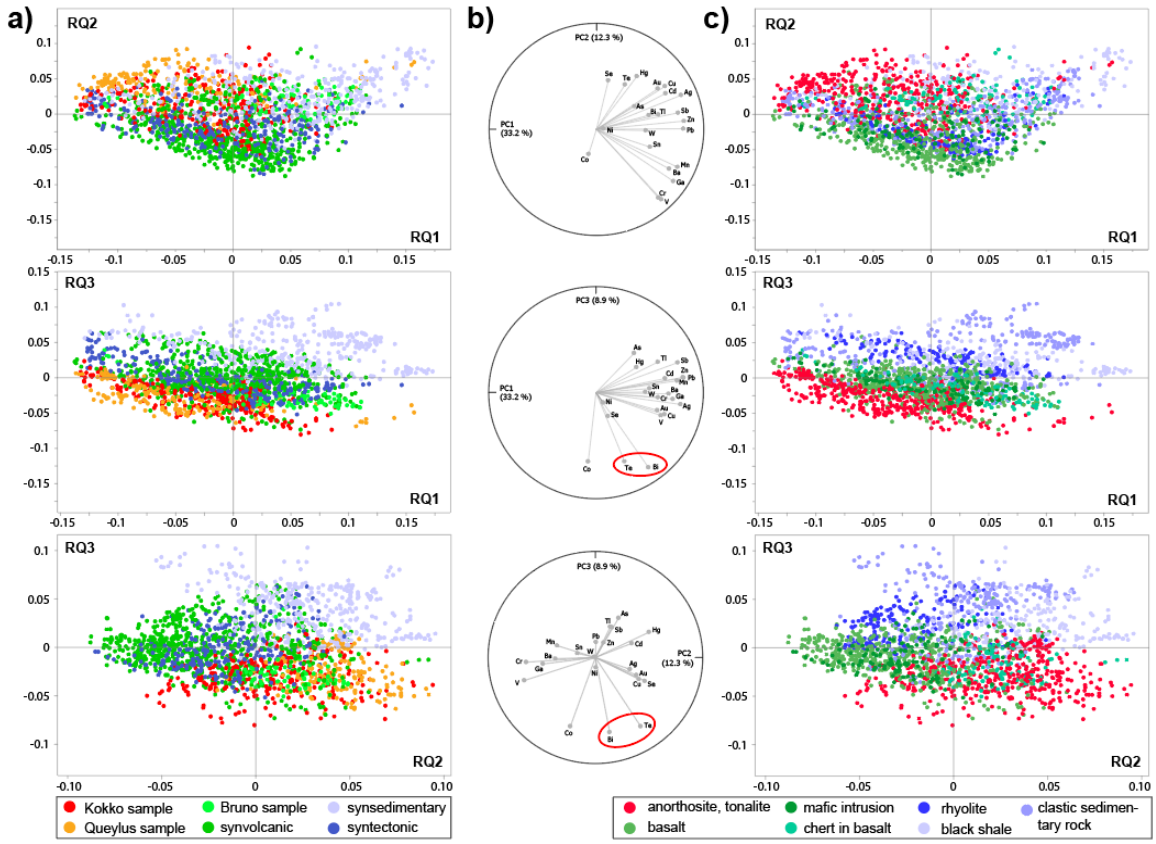


**Figure 10:** Results of principal component analysis (PCA) performed using the DB3 dataset ($n$ = 1898) and the elements of interest as variables ($m$ = 22). The diagrams are displayed, from top to bottom, as a function of PC1 and PC2, PC1 and PC3, and PC2 and PC3. The dataset is displayed on binary diagrams using color codes that refer to the composition of the host rocks (a) and the depositional environment (c). The contribution of each variable is shown using circle diagrams (b).

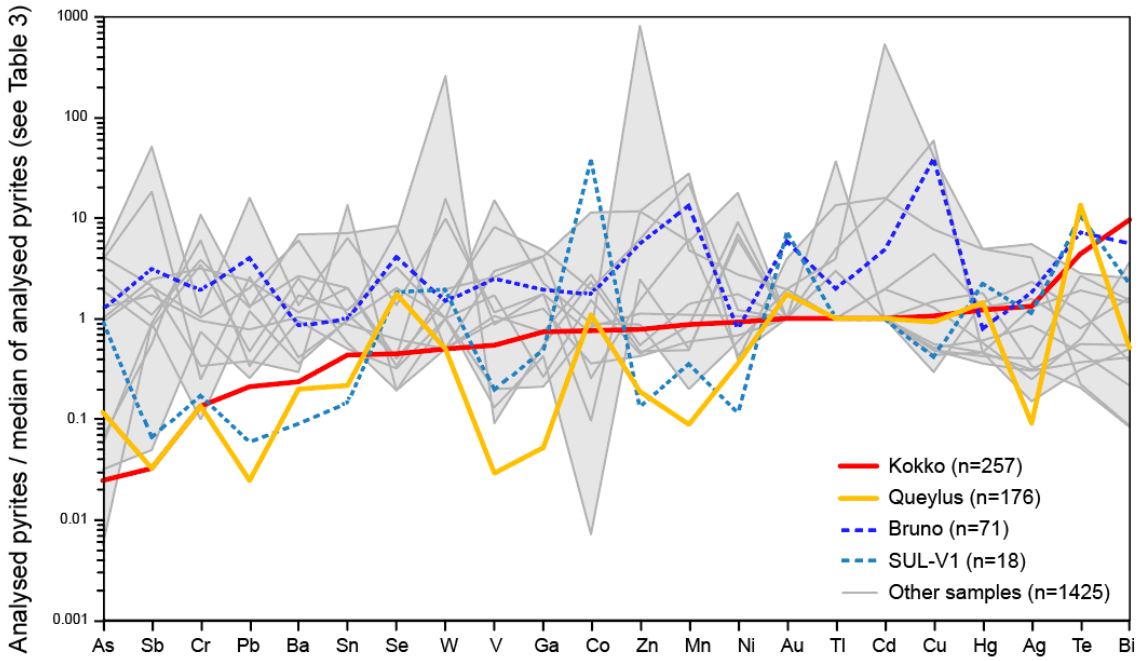


**Figure 11:** Multielement diagram for sulfide grains (for pyrite, chalcopyrite, and sphalerite analyses; with Fe-rich analyses discarded) of the DB3 dataset (*n* = 1947), normalized by the median values reported in Table 3. The elements are displayed in order of increasing abundance in the pyrites of the Kokko sample (red line). These pyrites are richer in Bi and Te and poorer in As, Sb, Cr, Pb, Ba, and Sn than the other pyrites considered. The pyrites from the Queylus sample display the same tendency as the Kokko sample with the exception of Bi. The pyrites from the old Bruneau mine (Bruno sample) and the nearby SUL-V1 sample are also enriched in Te and ±Bi.

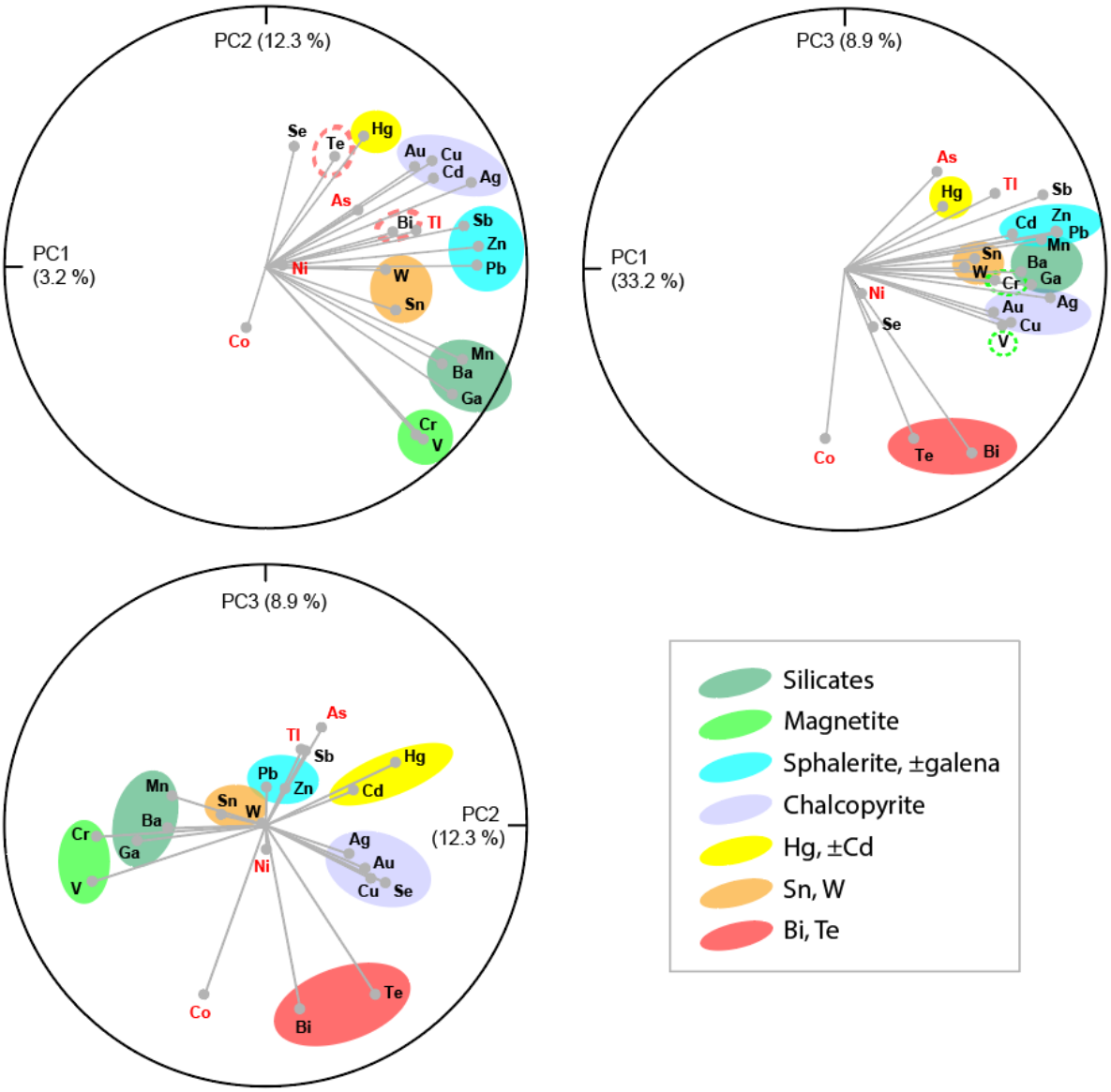


**Figure 12:** Zoom on the circle diagrams of Figure 10, obtained by principal component analysis (PCA) of the DB3 dataset ($n$ = 1898). The diagrams are displayed as a function of PC1 and PC2, PC1 and PC3, and PC2 and PC3. The color codes enhances the main positive correlations between elements.

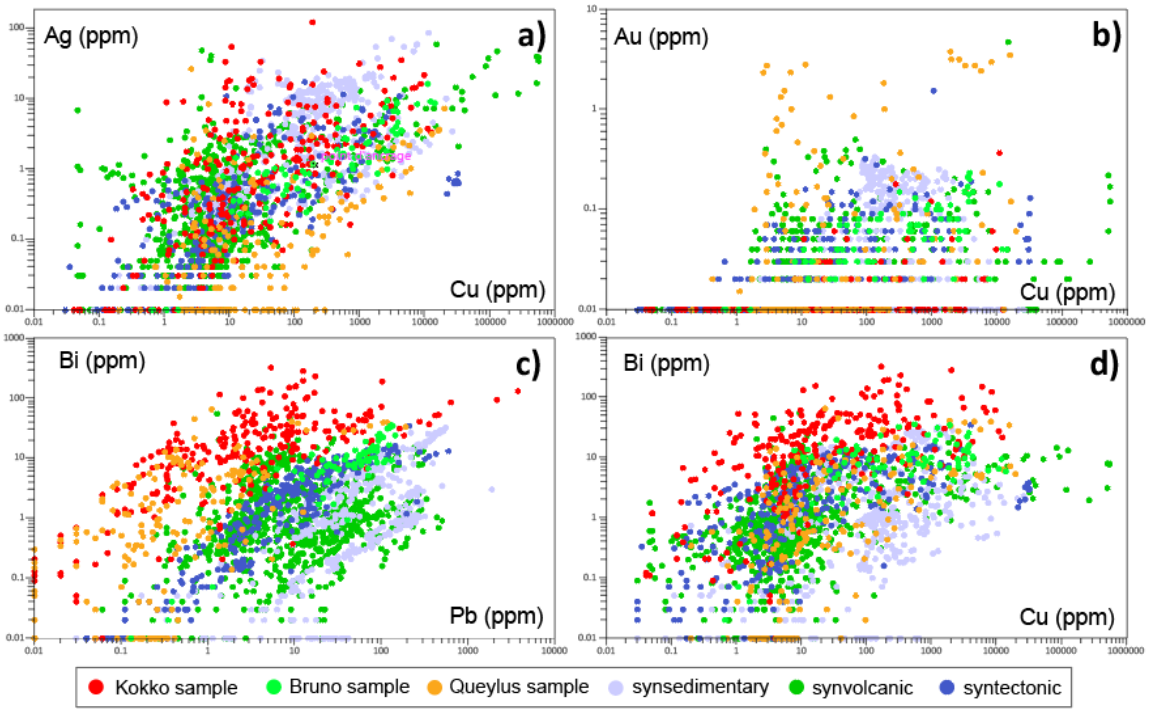


**Figure 13:** Ag vs Cu (a), Au vs Cu (b), Bi vs Pb (c), and Bi vs Cu (d) binary diagrams showing the pyrites and other sulfides of the DB3 dataset (*n* = 2145). The color code is designed to help the reader compare the chemistry of the pyrites from magmatic-hydrothermal systems (Kokko, Queylus, and Bruno samples) to those formed in other contexts.

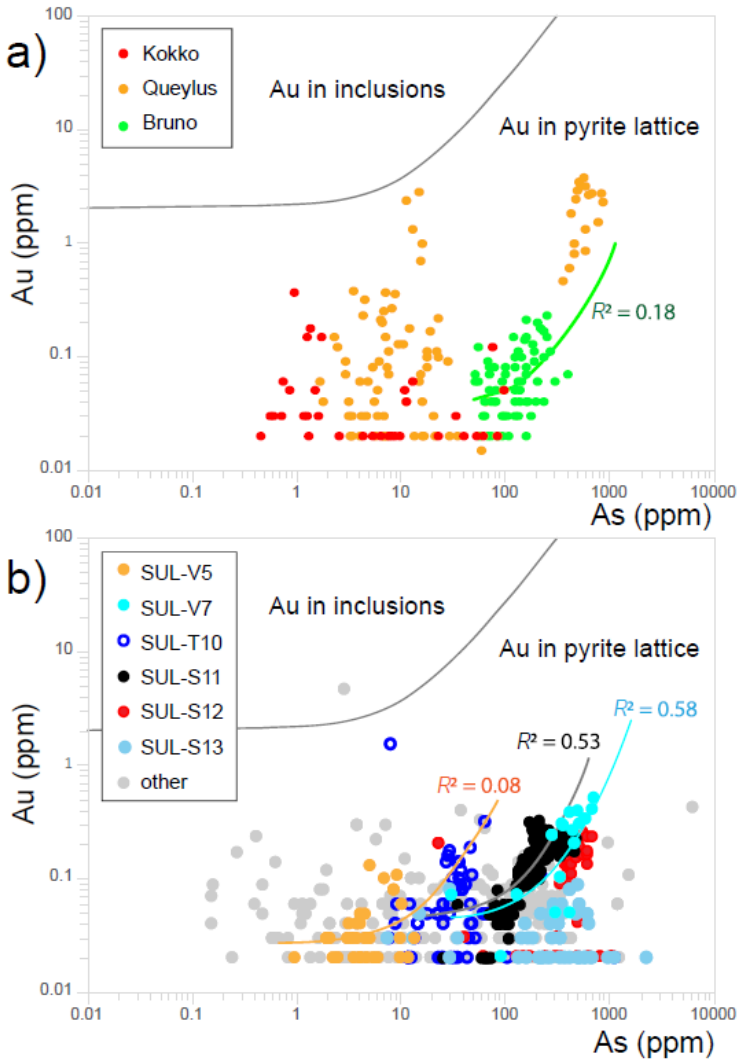


**Figure 14:** Diagram of Au solubility in pyrite as a function of As (Reich et al. 2005), displaying the analyses of the DB3 dataset for which Au is detected, i.e., Au > 0.1 ppm, *n* = 831. The samples are from magmatic-hydrothermal systems (a) and other environments (b). The color code (b) emphasizes the samples for which Au and As are correlated; the other samples are displayed in gray.

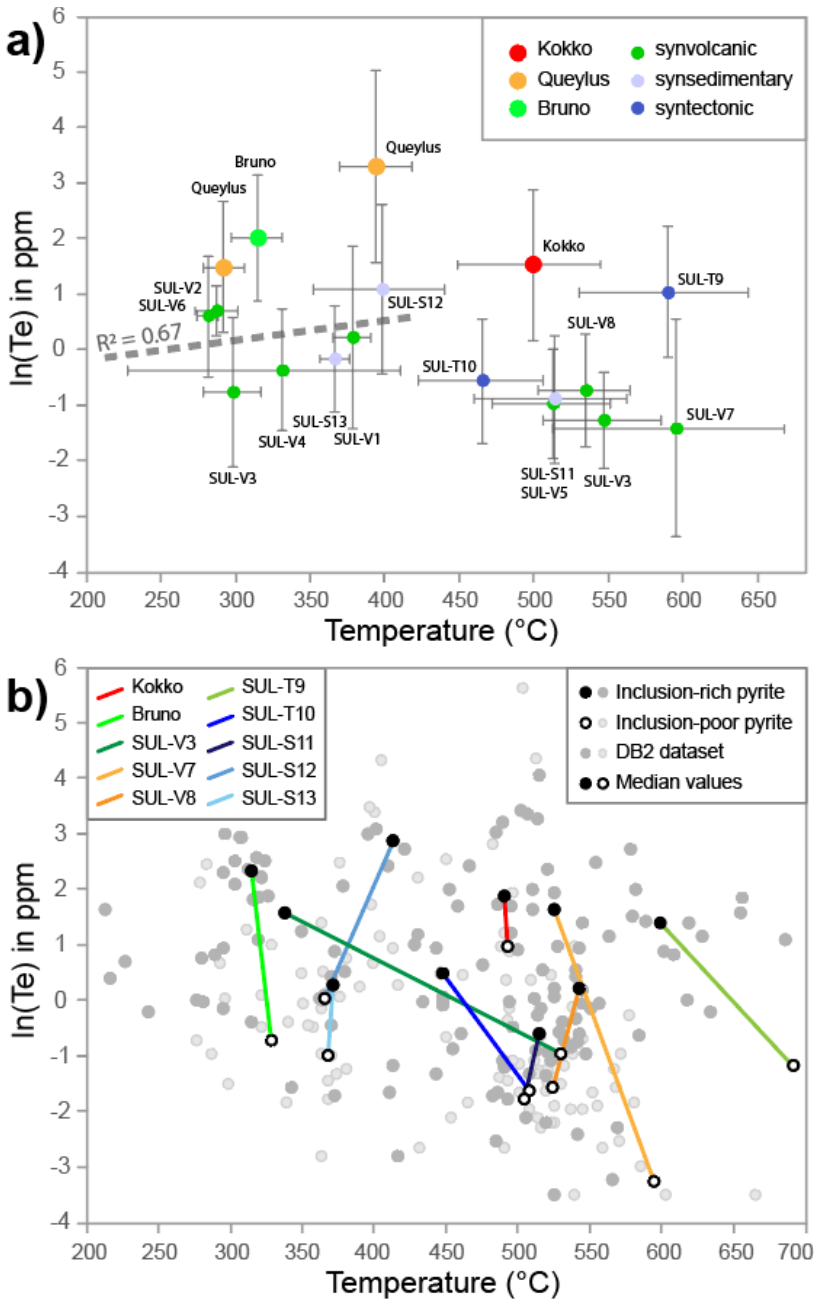


**Figure 15:** Binary diagram of ln(Te) vs temperature estimated using the Se-in-pyrite thermometer (Keith et al. 2018). The dots and error bars correspond to median and standard deviation, respectively, calculated using the DB3 dataset (*n* = 2145) (a). Two median values are calculated for the Queylus and SUL-V3 samples, in which Se has a bimodal distribution (a). The bottom diagram (b) shows median values calculated using the analyses of the DB2 dataset and for the samples that contain inclusion-rich and inclusion-poor pyrites (*n* = 188).

**Table 1:** Sample list and location

| Sample | UTMEU18 | UTMNU18 | Host rock | Pyrite origin | Formation, location |
|---|---|---|---|---|---|
| **Kokko** | 547443 | 5525432 | anorthosite | porphyry | Lac Doré Complex (Cu-Au Central Camp) |
| **Queylus** | 543739 | 5508354 | tonalite | porphyry (?) | Hydrothermal breccia in the rocks of the Chibougamau pluton |
| **Bruno** | 553459 | 5531754 | basalt | porphyry (?) | Bruneau Formation (old Cu-Au-Ag Bruneau mine) |
| **SUL-V1** | 553531 | 5531830 | basalt | synvolcanic | Bruneau Formation (near the old Bruneau mine) |
| **SUL-V2** | 535928 | 5544073 | basalt | synvolcanic | Bruneau Formation |
| **SUL-V3** | 535928 | 5544073 | basalt | synvolcanic | Bruneau Formation |
| **SUL-V4** | 538851 | 5534698 | basalt | synvolcanic | Bruneau Formation |
| **SUL-V5** | 553282 | 5550067 | basalt | synvolcanic | Bruneau or Obatogamau Formation, Barlow Fault (lower amphibolite facies) |
| **SUL-T9** | 556035 | 5550291 | mafic intrusion | syntectonic | Cummings sill along the Barlow Fault |
| **SUL-V6** | 515874 | 5510071 | chert in basalt | synvolcanic | Obtaogamau Formation (lower amphibolite facies due to contact metamorphism) |
| **SUL-V7** | 525920 | 5483935 | volcanoclastic | synvolcanic | Waconichi Formation |
| **SUL-V8** | 555392 | 5538504 | volcanoclastic | synvolcanic | Blondeau Formation |
| **SUL-T10** | 541675 | 5538540 | clastic sed. rock | syntectonic | Bordeleau Formation |
| **SUL-S11** | 559797 | 5539549 | clastic sed. rock | syn-sedimentary | Blondeau Formation |
| **SUL-S12** | 554987 | 5532695 | black shale | syn-sedimentary | Blondeau Formation |
| **SUL-S13** | 556925 | 5536272 | black shale | syn-sedimentary | Blondeau Formation |

**Table 2:** Main minerals observed as inclusions in pyrite and in the host rock

| Sample | Pl or Ab-Ep[a] | Qz | Ms | Bt | Chl | Amp | Spn | Cb | Mag |
|---|---|---|---|---|---|---|---|---|---|
| **Kokko** | X | | X | | X | | | | X |
| **Queylus** | X | X | X | X | | | | X | |
| **Bruno** | X | | | | X | X | X | | |
| **SUL-V1** | X | X | | | | X | X | | |
| **SUL-V2** | X | X | | | | X | X | | |
| **SUL-V3** | X | | X | | | X | X | | |
| **SUL-V4** | X | X | X | | X | X | X | X | X |
| **SUL-V5** | X | X | | X | X | X | X | X | |
| **SUL-T9** | X | | X | | | X | X | | |
| **SUL-V6** | X | X | X | | X | | | | |
| **SUL-V7** | X | X | X | | | | | X | |
| **SUL-V8** | X | X | X | | X | | | X | |
| **SUL-T10** | X | X | X | | | | X | | |
| **SUL-S11** | X | X | X | | X | | | X | |
| **SUL-S12** | | X | X | | | | | X | |
| **SUL-S13** | X | X | X | | X | | | X | |

[a] Mineral abbreviations stand for: albite (Ab), amphibole (Amp), biotite (Bt), carbonate (Cb), chlorite (Chl), epidote (Ep), magnetite (Mag), muscovite (Ms), plagioclase (Pl), quartz (Qz) and titanite (Spn).

**Table 3:** Median chemical composition of the studied pyrites (in ppm)

| Element | Median | Element | Median |
|---|---|---|---|
| **V** | 2.06 | **Cd** | 0.01 |
| **Cr** | 1.09 | **Sn** | 0.14 |
| **Mn** | 7.48 | **Sb** | 0.30 |
| **Co** | 429.53 | **Te** | 1.03 |
| **Ni** | 129.27 | **Ba** | 0.77 |
| **Cu** | 12.10 | **W** | 0.02 |
| **Zn** | 2.00 | **Au** | 0.01 |
| **Ga** | 0.19 | **Hg** | 0.28 |
| **As** | 86.93 | **Tl** | 0.01 |
| **Se** | 10.85 | **Pb** | 13.41 |
| **Ag** | 0.65 | **Bi** | 1.56 |